https://doi.org/10.5194/egusphere-2026-6344
Preprint. Discussion started: 9 November 2026
© Author(s) 2026. CC BY 4.0 License.

Estimating planetary boundary layer height using Doppler lidar

Petra Duff[1], Zen Mariani[2], Elisabeth Galarneau[3], Sylvie Leroyer[4], Audrey Lauer[4], Samir Singh[5], Mark Gordon[5], Robert Crawford[2], and Kimberly Strong[1]

[1]Department of Physics, University of Toronto, 255 Huron St., Toronto, Ontario, M5S 1A7, Canada
[2]Earth Observation and Research Section, Environment and Climate Change Canada, 4905 Dufferin St., Toronto, Ontario, M3H 5T6, Canada
[3]Earth Science Research and Integration, Environment and Climate Change Canada, 4905 Dufferin St., Toronto, Ontario, M3H 5T4, Canada
[4]Terrestrial Environment Numerical Prediction Research Division, Environment and Climate Change Canada, 2121 Transcanada Hwy, Dorval, Quebec, H9P 1J3, Canada
[5]Department of Earth and Space Science and Engineering, York University, 4700 Keele St., Toronto, Ontario, M3J 1P3, Canada

Correspondence: Petra Duff (petra.duff@utoronto.ca)

Abstract. The planetary boundary layer height (PBLh) is a key parameter in atmospheric modeling and observational applications, but is inconsistently defined in the literature and lacks a large, global ensemble of observations. Doppler lidar observational datasets, with high temporal resolution and deployability, provide an opportunity for long-term, high vertical and temporal resolution PBLh estimates to improve our understanding of atmospheric mixing. Using data collected by the Southern Ontario LIDar (SOLID) Mesonet, a network of Doppler lidar sites spanning 500 km across Southern Ontario, Canada, we present three methods for estimating the PBLh from Doppler lidar vertical wind speed and aerosol backscatter observations. We perform comparisons with PBLh estimates from the Global Environment Multiscale (GEM) model, the ECMWF Reanalysis 5 (ERA5), and nearby radiosonde flights at the Buffalo International Airport, New York, USA. We identify the vertical wind variance threshold method to be the estimate with the highest consistency with expected PBLh values and variation, comparisons to numerical and radiosonde measurement-derived estimates, and least sensitivity to noise in observations. However, each of the methods presented here show a general consistency with theoretical expectations and comparisons in appropriate conditions, affirming the validity of Doppler lidar-derived PBLh estimates in Southern Ontario.

1 Introduction

The planetary boundary layer (PBL) is typically defined to be the layer of the troposphere which is directly affected by the Earth's surface and its interaction with large-scale atmospheric flow. It is characterized by turbulent winds and a strong capping inversion that often causes pollutants produced at the surface to be both well-mixed and trapped within the layer (Stull, 2012). As a result, the study of atmospheric processes in the PBL and the impact of the PBL's structure thereon is significant to human

https://doi.org/10.5194/egusphere-2026-6344
Preprint. Discussion started: 9 November 2026
© Author(s) 2026. CC BY 4.0 License.

life and our understanding of anthropogenic climate and atmospheric change. Planetary boundary layer height (PBLh) is a key parameter in describing atmospheric dynamics for atmospheric modelling and observation. Uncertainties in model estimates of PBLh can introduce errors into modelled surface pollutant concentration estimates (Park et al., 2022; Davies et al., 2007; Zhao et al., 2019). Corrections to modeled PBLh using assimilated observations have been shown to improve simulated atmospheric parameters and pollutant concentrations compared to observations (Tangborn et al., 2021; Oak et al., 2019), indicating that increasing long-term, high temporal resolution observations of the PBLh globally is of a high priority to understanding air pollution in the PBL. Understanding temporal and spatial changes in the PBLh also allow us to better understand and predict pollutant levels in the PBL and at the surface. Temporal and spatial differences in PBLh have been shown to have impacts on the vertical distribution and surface concentrations of atmospheric pollutants (Foskinis et al., 2024; Du et al., 2013; Quan et al., 2013; Kim et al., 2007), especially in urban environments where anthropogenic heat flux feedbacks affect PBLh evolution in complex ways (Barlow et al., 2015; Wang et al., 2021).

Despite this importance, the PBLh lacks a consistent definition and a large ensemble of long-term, continuous observations. One way that the PBLh can be defined is as the height up to which atmospheric turbulence responds to surface-level forcings on short timescales (Stull, 2012). This is the definition we will use in this work. However, other definitions include: the altitude of the lowest temperature inversion layer (Heffter, 1980), the height of a layer of turbulent mixing leading to redistribution of atmospheric constituents and heat on short time scales (Anderson and Neff, 2008; Seibert et al., 2000), the height at which turbulent momentum and heat fluxes drop rapidly in the transition to free atmosphere (Anderson and Neff, 2008), and the height at which winds approach geostrophic behaviour (Liu and Liang, 2010; Stull, 2012). There is no direct method of measuring the PBLh, so the variation in these definitions comes from their dependence on the choice of measurement techniques and proxy atmospheric quantities used to observe the PBL and estimate its height. Such measurement techniques include identifying the altitudes of sharp aerosol gradients using ground-based instruments like back-scattering lidar (Lewis et al., 2013; Vaisala, 2010), similarly identifying gradients in other well-mixed atmospheric constituents such as ozone or water vapour using balloon-borne instruments (Anderson and Neff, 2008; Duncan Jr et al., 2022), and acoustic detection of sharp decreases in thermal fluctuations using sodar (Emeis et al., 2008). These "profile" methods have been developed in addition to a number of surface-based methods (dependent on parameters such as roughness length and turbulence kinetic energy) that are less preferred but often applied in modelling (Aliabadi et al., 2016; Zadra, 2014).

Methods using radiosonde measurements are typically considered to be the most reliable and therefore often serve as benchmarks for comparison for other remote sensing methods (Scarino et al., 2014; Aliabadi et al., 2016; Su et al., 2020) and training machine-learning models (Krishnamurthy et al., 2023). There exists variation even between these methods, however. The number of possible estimation techniques from just radiosonde observations include setting the PBLh at the height of the first inversion layer as identified using the virtual potential temperature gradient (Heffter, 1980), the minimum gradient in relative humidity (Tucker et al., 2009), the height of stability of a rising air parcel (Liu and Liang, 2010), and the height of a critical bulk Richardson number (Zilitinkevich and Baklanov, 2002). It must also be noted that turbulence in stable boundary layers is not always uniform and that the PBLh is not necessarily equivalent to the inversion height, as may be determined from radiosonde data (Balsley et al., 2006; Beyrich, 1997). Furthermore, radiosonde data are severely limited by the ability to per-

https://doi.org/10.5194/egusphere-2026-6344
Preprint. Discussion started: 9 November 2026
© Author(s) 2026. CC BY 4.0 License.

form launches, which is not possible in many environments (such as urban centres) and during periods of high surface winds. Temporal resolution is also naturally constrained to times of the launches themselves, which tend to only occur a maximum of twice daily at sites with regular launches, therefore inhibiting our ability to observe diurnal variations in the PBLh.

Doppler lidar presents an opportunity to provide complementary long-term, consistent, and widespread datasets in a comparable measurement space to radiosonde observations. Doppler lidar-derived wind profiles agree well with radiosondes (Mariani et al., 2020) and the wind velocity and aerosol backscatter measurements have been shown to accurately estimate the PBLh as compared to radiosonde measurements (Tucker et al., 2009; Schween et al., 2014). Additionally, there are a number of advantages of Doppler lidar systems over radiosondes including but not limited to higher temporal resolution and ability to measure in complex terrain and weather conditions (Tucker et al., 2009; Mariani et al., 2020, 2026).

The Southern Ontario LIDar (SOLID) Mesonet is a mixed-design network of Doppler lidars and complementary instruments deployed in and around Toronto, Ontario, Canada (Mariani et al., 2026). The study period began in November 2022 with the deployment of a Doppler lidar next to one of the runways at the Toronto Pearson International Airport and has since expanded to eight sites around Southern Ontario. The Mesonet aims to complement radiosonde observations via wind profiling and provides operational forecasters with continuous, near-real time observations.

In this paper, we present three methods for estimating the PBLh using Doppler lidar data collected by the SOLID Mesonet and test their robustness and reliability compared to its theoretical understanding in addition to radiosonde observations and model estimates. As mentioned above, we adopt the definition of the PBL characterized by turbulence as forced by surface topography. Within this definition, we use both backscatter and vertical wind measurements from the SOLID Mesonet to estimate the PBLh: with the former we identify maximal temporal variance in aerosol backscatter to pinpoint turbulent processes characteristic of the top of the PBL, and with the latter we identify the transition from the turbulent PBL to the free atmosphere, using both a threshold method and a minimized gradient method to identify drop-offs in vertical wind speed variance. These algorithms are described in Section 2.2. They are applied to long-term datasets at five sites in the SOLID Mesonet, chosen based on data availability. The resultant PBLh values are then compared to Global Environment Multiscale (GEM) model (Côté et al., 1998) output and ERA5 reanalysis (Hersbach et al., 2020) data, along with limited comparisons to radiosonde observations from launches in Buffalo, NY, United States by the United States National Oceanic and Atmospheric Administration (NOAA). For comparisons, we focus on the PBLh during the period from January to March 2024, for its coincidence with the sampling period of the Study of Winter Air Pollution in Toronto (SWAPIT) (ECCC, 2024). SWAPIT was a six-week measurement campaign conducted by Environment and Climate Change Canada (ECCC) in downtown Toronto, Ontario, investigating wintertime urban air pollutants. This study aims to support work using SWAPIT observations to understand urban wintertime air quality and atmospheric composition.

In Section 2, we introduce the SOLID Mesonet Doppler lidar dataset and the instruments used for observation, describe the PBLh estimation algorithms for the Doppler lidar and radiosonde data used here in addition to those of GEM and ERA5.In Section 3, we present the Doppler lidar-derived PBLh estimates for each SOLID measurement site and compare to GEM, ERA5, and radiosonde estimates. These results are discussed in Section 4, and conclusions are presented in Section 5.

https://doi.org/10.5194/egusphere-2026-6344
Preprint. Discussion started: 9 November 2026
© Author(s) 2026. CC BY 4.0 License.

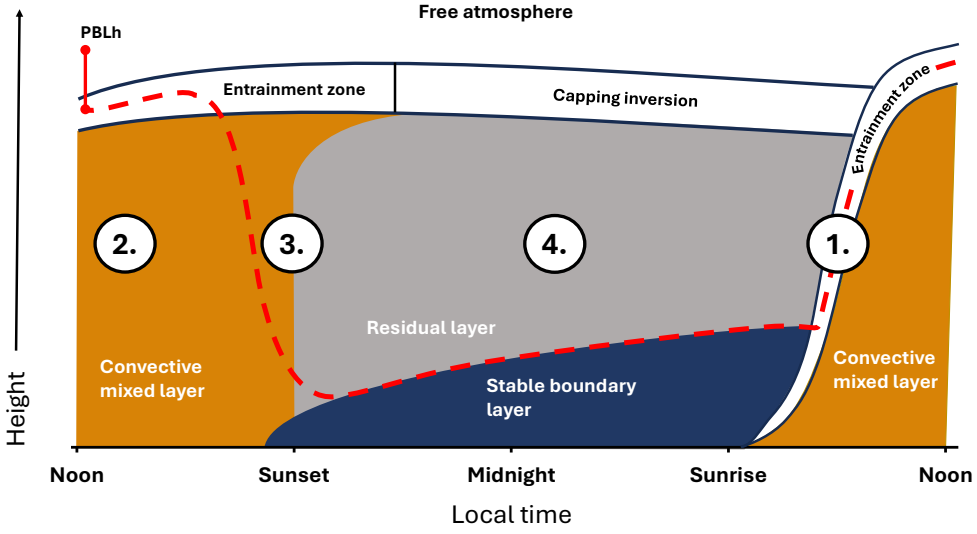


Figure 1. An idealized typical diurnal evolution of the PBL during fair weather in the summer over land. Four phases are numbered for clarity: 1, the growth of the PBL via entrainment from turbulence caused by surface heating by the sun; 2, the daytime convective mixed layer characterized by homogenous temperature and constituent profiles; 3, the collapse of the convective PBL; and 4, the growth of the stable PBL overnight, with aerosols left suspended in the residual layer. The associated PBLh is indicated with a dashed red line. Adapted from Stull (2012).

1.1 Background

A simplified diagram of the typical diurnal evolution of the PBL in fair-weather summertime conditions over land is shown in Fig. 1, after Stull (2012). Four phases are labeled for clarity. Generally, the PBL enters the first phase after sunrise, characterized by solar heating of the surface that produces turbulence via updrafts. The PBL is fed by a process called "entrainment" caused by this turbulence, allowing it to grow in depth as air from the free atmosphere is pulled into the PBL. We call the atmospheric layer in which this process occurs the *entrainment zone* (Cohn and Angevine, 2000). During the day, in phase two, the PBL is convectively unstable and well-mixed: temperature and atmospheric constituent profiles are typically homogenous, and experience a sharp dropoff at the top of the PBL.

Phase 3 sees the convective PBL collapse with sunset as the ground cools. Replacing it, the stable PBL begins to form near the surface due to radiative cooling. Overnight (phase 4), this radiative cooling remains relatively constant, causing the stable PBL to slowly "grow" in depth and strength as air further aloft is cooled and becomes stable. Surface warming from sunrise then causes turbulent entrainment to overtake it and start the cycle anew. The final transition is not immediate, however: the overnight statically stable PBL acts as a capping inversion layer that inhibits the growth of the morning covnective PBL. Note

https://doi.org/10.5194/egusphere-2026-6344
Preprint. Discussion started: 9 November 2026
© Author(s) 2026. CC BY 4.0 License.

that aerosols and other atmospheric constituents are left behind in the statically stable "residual layer" in phase 4. Without turbulence, the air aloft is no longer coupled to surface forcings.

The stable PBLh is particularly difficult to observe, given that the sharp gradients characteristic of the convective PBL top are not present (Tucker et al., 2009; Aliabadi et al., 2016) and synoptic weather patterns or other phenomena like supergeostrophic winds that would otherwise not occur or have significant impacts in turbulent conditions can modify its structure. This limits our ability to observe nighttime PBLh evolution. Realistically, however, nighttime conditions can also be weakly stable or neutral. The evolution of the PBLh can deviate from this idealized model with changes in season, environment, and latitude, often with a stronger and longer-lasting nocturnal stable PBL in wintertime, but these phases described above remain generally applicable as long as there is a disparity in daytime and nighttime temperatures with radiative warming of the surface from the sun (Stull, 2012).

2 Methodology

2.1 SOLID Mesonet Doppler lidar data

The SOLID Mesonet is a network of Doppler lidar measurement sites spanning 500 km across Southern Ontario (Mariani et al., 2026). The first of these sites was installed at Toronto Pearson International Airport (hereafter referred to by the site code CYYZ) in November 2022, as mentioned above. The rest have been deployed intermittently since, with the latest instrument having been installed at Ottawa International Airport (site code CYOW) in September 2024.

Doppler lidar measures line-of-sight wind speed by measuring the Doppler shift of a backscattered pulse of infrared radiation, as a consequence of interaction with moving air particles. The Mesonet is of a mixed network design, with five of the instruments being Halo STREAMline XR+ models and three being Leosphere 100S Windcube models. The Halo models are the only instruments considered in this work due to data availability, and are deployed at five sites: CYOW, CYYZ, Ontario Ministry of the Environment, Conservation, and Parks rooftop (site code MECP) near Highway 401 in Toronto, University of Toronto Scarborough (site code UTSC) in Scarborough, and Western University (site code WEST) in London. These sites are listed alongside their location, altitude, deployment date, and region type in Table 1, and are shown on a map in Fig. 2 along with timelines of data availability for each site.

These lidars operate autonomously 24/7 in all weather conditions (except during periods of heavy precipitation when its beam is attenuated). The theoretical maximum range of the instruments extends up to 10 km, however their actual range is limited by the number of aerosols in the atmosphere, as cleaner air provides limited targets and therefore reduced signal (Fast and Darby, 2004). Vertical wind velocity scans are taken using a five-minute zenith-viewing stare mode scan every 10 minutes, along with alternate modes for horizontal velocity measurements. Details concerning these scan modes and the reliability, accuracy, and maintenance of SOLID Mesonet data products can be found in Mariani et al. (2026).

Multi-year, multi-site comparisons indicate excellent agreement between Halo lidar wind profile measurements and other datasets, with low biases shown against radiosonde measurements and numerical model outputs (Mariani et al., 2020). Comparisons against radar also confirm lidar's ability to detect wind shears and stratified wind layers (Mariani et al., 2018a), as

https://doi.org/10.5194/egusphere-2026-6344
Preprint. Discussion started: 9 November 2026
© Author(s) 2026. CC BY 4.0 License.



well as low-level jets, enhanced convection, cloud base height, and fast-moving meteorological features such as the lake breeze front (Mariani et al., 2018b). This precision makes Doppler lidar promising for tracking potentially complex evolution of the turbulent boundary layer, especially in stable conditions where the influence of horizontal heterogeneity may be greater (Aliabadi et al., 2016). The disadvantage of this system with regards to PBLh estimation is that the vertical range of the commercial instruments in use in the Mesonet is limited by aerosol layer distribution in the PBL: the low-energy laser pulses typical of Doppler lidar systems cannot penetrate optical depths typical of thick clouds or fog, and so for our purposes here we limit the Doppler lidar dataset to cloudless conditions. PBLh estimation can also be affected by noisy data above the maximum vertical range due to these limitations, for which we apply specialized quality-control procedures described in the following section.

SOLID Mesonet data are quality-controlled (as described in Mariani et al. (2018b)) and delivered to forecasters in real-time, with new profiles publicly available every 10 minutes online at http://hiwr.ca/mesonet.php and on ECCC's internal data management system provided to operational forecasters. This includes raw data and processed products for horizontal wind profiles (u, v), vertical wind profiles (w), and aerosol backscatter. Cloud base height and PBLh are also calculated in real-time using the methods presented here, but not publicly available.

Table 1. Locations, deployment date, and description of the region's environment for each SOLID Mesonet site considered in this study: Ottawa International Airport (CYOW); Toronto Pearson International Airport (CYYZ); Ontario Ministry of the Environment, Conservation, and Parks near Highway 401 (MECP); University of Toronto, Scarborough (UTSC), and Western University Field Station (WEST).

Site	Lat (°)	Lon (°)	Altitude (m a.s.l.)	Altitude (m AGL)	Deployment date	Region type
CYOW	45.3273	-75.6637	112	0	September 7, 2024	Airport hangars
UTSC	43.7835	-79.1880	152	21	October 20, 2023	Suburban
MECP	43.7109	-79.5422	141	10	November 6, 2023	Urban, highways
CYYZ	43.6660	-79.6062	163	1	November 15 2022	Airport runways
WEST	43.0753	-81.3373	280	2	October 17, 2023	Farmland

2.2 PBLh estimation using Doppler lidar data

Definitions of the PBL and the PBLh vary according to both application and observation techniques. While different definitions may produce similar results under certain meteorological and topographical conditions, others might introduce biases in estimates across the various methods. As mentioned above, here we focus on a turbulence-based definition of the PBLh. That is, as per Fig. 1, the algorithms presented here are designed to track the evolution of the convective PBL (or mixed layer) during the day and the existence of any weak turbulence in weak stably stratified or neutrally stable PBL conditions at night. Given that a strongly stable PBL exhibits no turbulence, we are not able to track the evolution of the stable nocturnal PBLh. This is as opposed to, for example, scattering lidar-based estimation methods that may instead track residual layer evolution overnight (Aliabadi et al., 2016; Park et al., 2022), or microwave radiometer methods that identify the stable PBLh using temperature inversion identification (de Arruda Moreira et al., 2018).

https://doi.org/10.5194/egusphere-2026-6344
Preprint. Discussion started: 9 November 2026
© Author(s) 2026. CC BY 4.0 License.

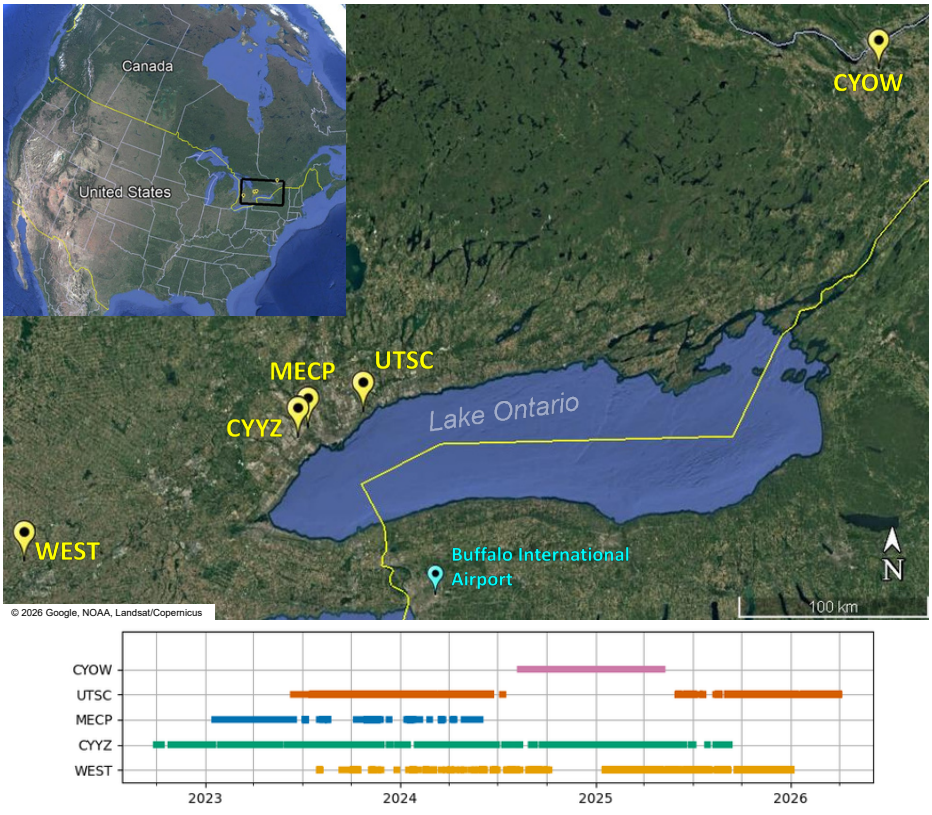


Figure 2. The SOLID Mesonet. Above: Map indicating locations of the SOLID Mesonet Halo model lidar measurement sites considered in this study: Ottawa International Airport (CYOW); Toronto Pearson International Airport (CYYZ); Ontario Ministry of the Environment, Conservation, and Parks near Highway 401 (MECP); University of Toronto, Scarborough (UTSC), and Western University Field Station (WEST). Buffalo Niagara International Airport is also indicated, as the location of radiosonde launches used in this study for comparison. Below: Timelines of SOLID Mesonet data used in this study, by site. Gaps in observations are due to instrument failures or poor data quality.

In this study, we investigate three methods for deriving the PBLh from two geophysical variables measured by Doppler lidar. The first method uses measurements of the aerosol backscatter coefficient, β. The entrainment zone, as described in Section 1.1, is also inconsistently defined, but is considered to be colocated with the PBLh in convective conditions and is characterized by temporally variable fluctuations in aerosol concentrations (Emeis et al., 2008). We therefore set the PBLh estimate to be the height at which the variance in the aerosol backscatter coefficient β is maximized, which we estimate as being the height of the entrainment zone (under the assumption that the thickness of the entrainment zone can be neglected). This estimate will hereafter be referred to as $h_{DL,\beta}$.

The aerosol backscatter variance is computed after the method of Schween et al. (2014) for computing vertical wind speed standard deviations: for every five minutes, the variance of the preceding 15 minutes and following 15 minutes is found. That is, the variance is found for a rolling 30-minute window centered on every five minutes. The time window length is chosen

https://doi.org/10.5194/egusphere-2026-6344
Preprint. Discussion started: 9 November 2026
© Author(s) 2026. CC BY 4.0 License.

based on the idea that it takes 16 min for a convective plume with average ascent speed of 1 ms^{-1} to travel through a PBL of 1 km height. This produces a total variance estimate that includes correlated and uncorrelated components; the uncorrelated components are removed as in Lenschow et al. (2000) to leave the correlated component, or the aerosol backscatter variance σ_β^2.

There are, however, limitations to the method. Doppler lidar data, specifically, can be suboptimal for the measurement of aerosol backscatter profiles: the coherent Doppler lidar range function is more complicated than direct detection (Frehlich and Kavaya, 1991) and depends highly on atmospheric conditions and aerosol concentrations (Rye, 1981; Belmonte and Rye, 2000). Additionally, the presence of pollution plumes can interfere with the lidar's zenith beam (Tucker et al., 2009), which is a risk in urban settings (often characterized by localized emission sources). Finally, because of the assumptions made in this method relating to the presence of the entrainment zone, it is typically only considered suitable for unstable PBL conditions (Emeis et al., 2008). This further limits its efficacy in higher-latitude locations like Southern Ontario that can experience stable PBL conditions throughout winter months, in addition to unreliable estimates at night. In the case of convective conditions, however, it can potentially produce a highly reliable estimate (Hennemuth and Lammert, 2006; Liu et al., 2021), and so is still considered here for comparisons to the following two methods.

PBLh estimates are also obtained using two methods using vertical wind speed observations from Doppler lidar. To do this, we consider that the vertical size of a plume undergoing homogenous turbulent motion is proportional to the vertical wind speed standard deviation σ_w (Taylor, 1935). We can therefore use σ_w or, in this case, σ_w^2 to characterize vertical mixing. Values of σ_w^2 that indicate a drop in turbulence at the cap of the PBL as it transitions into the free atmosphere can then be used to produce an estimate of the PBLh.

For the first of our two w-based methods, we define the PBLh to be the height at which σ_w^2, beginning at the highest altitude and scanning down, passes above a certain threshold, as in Tucker et al. (2009). Vertical wind speed variances are computed according to Schween et al. (2014) and Lenschow et al. (2000) as described for $h_{DL,\beta}$ above: using rolling 30-minute windows every five minutes. The variance threshold is chosen for our dataset to be 0.04 $\mathrm{m}^2/\mathrm{s}^2$ based on the threshold chosen for similar regions (Tucker et al., 2009). This estimate will be hereafter referred to as $h_{DL,wt}$. While this method is typical for Doppler lidar-derived wind estimates (Tucker et al., 2009; Schween et al., 2014; Park et al., 2022), the significant drawback rests in the somewhat arbitrary choice of threshold. Because the optimal threshold value may depend on meteorological conditions at the measurement site, there may exist a bias across instrument locations if the choice made here is more appropriate for some than others.

Finally, we developed a novel PBLh estimation method by minimizing the vertical gradient in the vertical wind velocity variance, identifying the point where turbulence drops significantly in the transition to the free atmosphere. Here, we first compute the gradient of the vertical wind speed variance $\nabla\sigma_w^2$ and then apply a smoothing Savitsky-Golay filter. Note that in cases of highly variable observations, this filter may not converge. In these cases, the observation is left out of the final $h_{DL,wg}$ estimate. We then set the PBLh to be the first local minimum scanning upward from the ground, using `scipy`'s peak-finding method. This is done with the understanding that observations made by the Doppler lidar become noisier above the mixed layer or residual layers with the decrease in aerosol concentrations, possibly introducing extreme gradients with noise. Identifying

https://doi.org/10.5194/egusphere-2026-6344
Preprint. Discussion started: 9 November 2026
© Author(s) 2026. CC BY 4.0 License.

Table 2. Summary of quality control procedures applied to data before estimating PBLh.

Quality control step	Parameter	Filter threshold	Filter method
SNR filter	SNR (w, β)	1.008	All datapoints with lower SNR removed
"Jump" removal	Consecutive differences in w, over altitude	3.0 m/s within 3 m and 5.0 m/s within 6 m	All datapoints above jumps in altitude removed
Large value filtering	w	5.0 m/s	All datapoints with higher w removed
Outlier filtering	w, β	$Q1 - 1.5IQR$, $Q1 + 1.5IQR$	All datapoints above or below outlier thresholds removed in 30-min windows every 5 min
Uncorrelated variance removal	$\sigma_w^2, \sigma_\beta^2$	N/A	Uncorrelated variance component removed after Lenschow et al. (2000).
Cloudless conditions	β	-4.7 dB	All datapoints with lower β removed

the first peak from the ground was found through testing to most reliably capture sharp decreases in turbulence expected at the PBLh.

As both of these w-based methods rely on turbulence within the PBL, only estimates made in turbulent or weakly turbulent conditions are considered. That is, estimates in conditions where σ_w^2 is less than the threshold value $\sigma_w^2 = 0.04$ at the lowest range gate are discarded. The PBLh in nocturnal conditions is therefore the height of stably stratified layers or low-level jets in turbulent conditions, and we are unable to precisely track the evolution of the nocturnal stable PBL.

2.3 Quality control

We perform several quality-control procedures on SOLID Mesonet data before applying the above PBLh estimation algorithms. The following is summarized in Table 2. We first apply a signal-to-noise ratio (SNR) filter to raw w and β datasets, removing data points with SNR values ≤ 1.008 after Mariani et al. (2018b). We then apply filters to the vertical wind speed data to correct for limited signal above the well-mixed PBL, where low aerosol concentrations cause noisy observations that can introduce non-physical wind variance values that may skew estimates. This is corrected by identifying large (nonphysical) "jumps" in wind speed values and removing them, and further removing all data above altitudes where long series of jumps can be found. We additionally apply an outlier filtering algorithm after Lenschow et al. (2000) to remove any noisy observations remaining after the previous two measures. Finally, due to the aerosol distribution-based limitations to Doppler lidar discussed above, data are limited to cloudless conditions. This is done by filtering out all datapoints in which a cloud base height, defined as the altitude at which the aerosol backscatter coefficient β rises above a threshold of -4.7 dB, can be detected. Hard minima and maxima are imposed at $h_{DL,x}^{min} = 100$ m and $h_{DL,x}^{max} = 2000$ based on theoretical expectations for the considered locations. The estimates revert to the hard caps minimally, if at all. For example, for the entire CYYZ time series, 5.3 % of $h_{DL,\beta}$ estimates can be found at the limits, 0.003 % of $h_{DL,wt}$, and none of $h_{DL,wg}$.

https://doi.org/10.5194/egusphere-2026-6344
Preprint. Discussion started: 9 November 2026
© Author(s) 2026. CC BY 4.0 License.

2.4 Comparison datasets

2.4.1 GEM

GEM is ECCC's operational weather forecast model, and outputs PBLh as one of its mixing parameters (McTaggart-Cowan et al., 2019), which we use as a point of comparison to the Doppler lidar PBLh products. The standard GEM PBLh estimates will be hereafter referred to as h_{GEM}. The model is typically run at a 2.5 km $\times$ 2.5 km horizontal resolution in Canada. However, this study also uses 250 m $\times$ 250 m horizontal resolution GEM outputs developed for complex, urbanized environments. Where current standard National short-range numerical weather prediction (NWP) at ECCC is performed at 2.5-km scale, 250-m scale experiments have shown better representation of urban landscapes, particularly with regards to thermodynamics and the urban heat island effect (Leroyer et al., 2022; Leroyer and Lauer, 2025). Given that most of the SOLID Mesonet sites are in or near urbanized areas, this makes PBLh estimates from 250-m GEM (hereafter $h_{GEM,250m}$) better suited to our purposes. However, given the computational expense of the model, outputs are currently only available for analysis during the months covering the SWAPIT period of January-March, 2024. As a result, we will limit our numerical comparisons to this period. The outputs have additionally been interpolated to the CYYZ location using bilinear interpolation. The reasons for interpolation and details of the interpolations applied for this study to ERA5 outputs are discussed further in Appendix A.

The PBLh algorithm for both versions of GEM uses separate schemes depending on the stability of the PBL, as determined by the value of the bulk Richardson number Ri_b in the surface layer. Inputs for PBLh estimates are extracted from levels surrounding the surface layer, defined as the layer located between the actual surface and the model's lowest prognostic levels. They are therefore primarily controlled by the model's surface scheme. At each time step, the surface scheme computes surface fluxes, which outputs the equilibrium height scale h_e. This is used as the empirical estimate of the PBLh.

In the stable case, where $Ri_b > 0$ in the surface layer, the estimate of the height scale h_e is computed based on surface fluxes. Surface fluxes are calculated by an iterative algorithm using inputs from the surface and the atmosphere. h_e is set to be the largest of four possible estimates:

$$h_e = max(h_1, h_2, h_3, h_4), \tag{1}$$

the expressions for which are as follows:

$$h_1 = \gamma \cdot (z_u + 10 \cdot z_{0m}) \tag{2}$$

for constant $\gamma = 1.2$, height of the model's lowest prognostic level z_u, and roughness length for momentum z_{0m};

$$h_2 = b\sqrt{\frac{\kappa u_* L}{|f|}} \tag{3}$$

for the von Karman constant $\kappa = 0.4$, the friction velocity u_*, the Monin-Obukhov length L, and the Coriolis parameter f;

$$h_3 = \frac{\gamma}{4a_s\beta} \cdot L \tag{4}$$

https://doi.org/10.5194/egusphere-2026-6344
Preprint. Discussion started: 9 November 2026
© Author(s) 2026. CC BY 4.0 License.

for constant $a_s = 12$, and constant $\beta = 1$; and finally

$$h_4 = h_{min} \tag{5}$$

for $h_{min} = 30$ m.

In the stable case, the surface stability function (used in the calculation of fluxes) depends weakly on h_e. The final calculated value of h_e is also capped at a maximum value of 1500 m for both the stable and unstable cases.

In the unstable case, the PBLh is found by the maximum of two estimates:

$$h = max(h_e, h_N) \tag{6}$$

The first estimate h_e, according to the surface flux height scale method above, is

$$h_e = 0.3\frac{u_*}{|f|} \tag{7}$$

The second, h_N, is found by calculating the profile of the squared buoyancy frequency N^2 as follows. For the profile of the square of the Brunt-Vaisala frequency $X = N^2$, we define

$$X = N^2 = \frac{g}{\theta_\nu}\frac{\partial \theta_\nu}{\partial z} \tag{8}$$

given the virtual potential temperature θ_ν. The thermodynamic level KCL is defined as the lowest (thermodynamic) model level in which X is positive. The geopotential height GZ at the thermodynamic level KCL is taken to be the profile-best estimate of the PBLh:

$$h_N = GZ(KCL) \tag{9}$$

Note that this method is only used in the unstable case, as if the entire profile is stable (i.e. $X > 0$ throughout the column) then KCL coincides with the lowest model level.

Additionally, current numerical weather prediction (NWP) model configurations consider five categories of surface: land, urban, water, sea-ice, and glaciers. Each of these receives the same atmospheric inputs from the first prognostic levels but has separate surface characteristics (e.g., roughness length) and surface state (e.g., surface temperature and moisture). As a result, there may be five separate estimates of h_e (and other parameters) within the same grid cell. An average grid-cell value is aggregated with weights according to the fractions of the surface area occupied by each type of surface:

$$h_e^a = \sum_{i=1}^{5} f_i \cdot h_e^i, \tag{10}$$

where the upper index a indicates the aggregated value, and f_i is the fraction of the grid-cell surface covered by surface type i. This value, h_e^a, is the final PBLh estimate produced for each grid cell.

https://doi.org/10.5194/egusphere-2026-6344
Preprint. Discussion started: 9 November 2026
© Author(s) 2026. CC BY 4.0 License.

2.4.2 ERA5

The European Centre for Medium-Range Weather Forecasts Reanalysis 5 (ERA5) has a spatial grid resolution of 31 km (0.28125 °) and a vertical resolution of 137 levels from the surface up to a height of 80km. We have interpolated the ERA5 PBLh product from this grid to the CYYZ location for more precise comparisons as discussed in Appendix A. The PBLh estimate computed by ERA5 follows Seidel et al. (2012), originally proposed by Vogelezang and Holtslag (1996), using the bulk Richardson number. The method was found to be optimal for application to radiosonde data, as well as reanalysis and climate model datasets. The PBLh in this case is defined as the height at which, while scanning upward from the surface, the bulk Richardson number passes a chosen threshold ($Ri_b = 0.25$). The bulk Richardson number for the layer from the surface up to a height h is computed according to:

$$Ri_b = h\frac{2f(s_{v,hbl} - s_{v,n})}{(s_{vhbl} + s_{v,n} - gh_{bl} - gz_n)|\Delta\mathbf{U}|^2}, \tag{11}$$

for the horizontal wind velocity at the boundary layer height

$$|\Delta\mathbf{U}|^2 = u_{hbl}^2 + v_{hbl}^2, \tag{12}$$

where u_{hbl} and v_{hbl} are the horizontal wind velocity components in the x and y, the virtual dry static energy for the lowest model level n

$$s_{v,n} = c_p T_n(1 + \varepsilon q_n) + gz_n, \tag{13}$$

and the virtual dry static energy at the boundary layer height

$$s_{v,hbl} = c_p T_{hbl}(1 + \varepsilon q_{hbl}) + gh_{bl} \tag{14}$$

from the temperature at each level i, T_i, the specific humidity at each level q_i, the specific heat capacity at a constant pressure c_p, the acceleration due to gravity g, and $\varepsilon = (R_{vap}/R_{dry}) - 1$, where R_{vap} and R_{dry} are the gas constants for water vapour and dry air, respectively.

3 Results

3.1 Doppler lidar estimates

3.1.1 Diurnal variation

The mean diurnal variation for each PBLh estimate ($h_{DL,\beta}$, $h_{DL,wt}$, and $h_{DL,wg}$) is shown by site in Fig. 3. Table 3 presents minima, maxima, and amplitudes (difference between maximum and minimum) in the diurnal mean for each dataset ($\pm 1\sigma$). Each of the two w-based estimates can be seen to, on average, qualitatively replicate the expected diurnal variation of the PBLh. At each site, we see the first phase of evolution clearly with PBLh rising gradually throughout the morning after sunrise as

https://doi.org/10.5194/egusphere-2026-6344
Preprint. Discussion started: 9 November 2026
© Author(s) 2026. CC BY 4.0 License.

Table 3. Diurnal mean PBLh maxima, minima, and amplitudes between maxima and minima ($\pm 1\sigma$) for each Doppler lidar estimate by site.

Site	Estimate	Maximum (m)	Minimum (m)	Amplitude (max-min; m)
	$h_{DL,\beta}$	578 ± 525	354 ± 378	223 ± 647
CYOW	$h_{DL,wt}$	662 ± 477	143 ± 56	519 ± 480
	$h_{DL,wg}$	711 ± 384	218 ± 11	494 ± 384
	$h_{DL,\beta}$	649 ± 490	465 ± 431	184 ± 653
UTSC	$h_{DL,wt}$	517 ± 334	172 ± 103	345 ± 349
	$h_{DL,wg}$	616 ± 374	272 ± 77	345 ± 382
	$h_{DL,\beta}$	610 ± 477	360 ± 359	250 ± 597
MECP	$h_{DL,wt}$	547 ± 337	174 ± 99	373 ± 351
	$h_{DL,wg}$	612 ± 356	258 ± 110	354 ± 372
	$h_{DL,\beta}$	691 ± 467	456 ± 444	236 ± 644
CYYZ	$h_{DL,wt}$	754 ± 464	206 ± 173	547 ± 496
	$h_{DL,wg}$	739 ± 395	309 ± 114	430 ± 411
	$h_{DL,\beta}$	735 ± 525	446 ± 429	290 ± 678
WEST	$h_{DL,wt}$	755 ± 475	157 ± 122	598 ± 490
	$h_{DL,wg}$	753 ± 476	290 ± 129	463 ± 493

growth from entrainment overpowers the capping power of the cooler, more stable nocturnal layer. The second phase seems to be better captured on average by $h_{DL,wg}$, remaining more consistent throughout the day at most sites than $h_{DL,wt}$, which has a tendency towards narrower daytime peaks. For example, the daily mean $h_{DL,wt}$ at UTSC peaks early in the day and begins to immediately decrease as opposed to the relatively plateau-shaped daytime $h_{DL,wg}$. At WEST, $h_{DL,wt}$ shows a later and more symmetric peak, but $h_{DL,wg}$ still shows a wider and flatter shape midday to late afternoon. However, values are otherwise reasonably consistent between the two estimates during the day: for example, the maximum average daily estimate at CYYZ (with maximum values typically occurring during convectively unstable periods during the day) is 754 ± 464 m for $h_{DL,wt}$ and 739 ± 395 m for $h_{DL,wg}$. Uncertainties in the mean (estimated as one standard deviation from the mean) for diurnal averages are large due to seasonal variations in the PBLh (discussed in the next section).

PBLh values drop to much lower heights, on average, during phase 3 collapse and phase 4 nocturnal boundary layer for $h_{DL,wt}$ than for $h_{DL,wg}$. This is reflected quantitatively in smaller overall daily amplitude in $h_{DL,wg}$ than in $h_{DL,wt}$. At CYYZ, $h_{DL,wg}$ has an average daily amplitude of 430 ± 411 m as opposed to a amplitude of 547 ± 495 m for $h_{DL,wt}$.

$h_{DL,\beta}$, conversely, does not track the expected variation as well. The latter portion of phase 1 is well-resolved on average across each site and phase 2 daytime values are consistent as expected, but phase 3 collapse is only somewhat observed and only at some sites. Overnight, $h_{DL,\beta}$ values rise back up to roughly daytime values and remain far above $h_{DL,wt}$ and $h_{DL,wg}$. CYYZ sees a comparably limited daily amplitude in $h_{DL,\beta}$ of 234 ± 644 and a minimum average PBLh (typically occurring

https://doi.org/10.5194/egusphere-2026-6344
Preprint. Discussion started: 9 November 2026
© Author(s) 2026. CC BY 4.0 License.

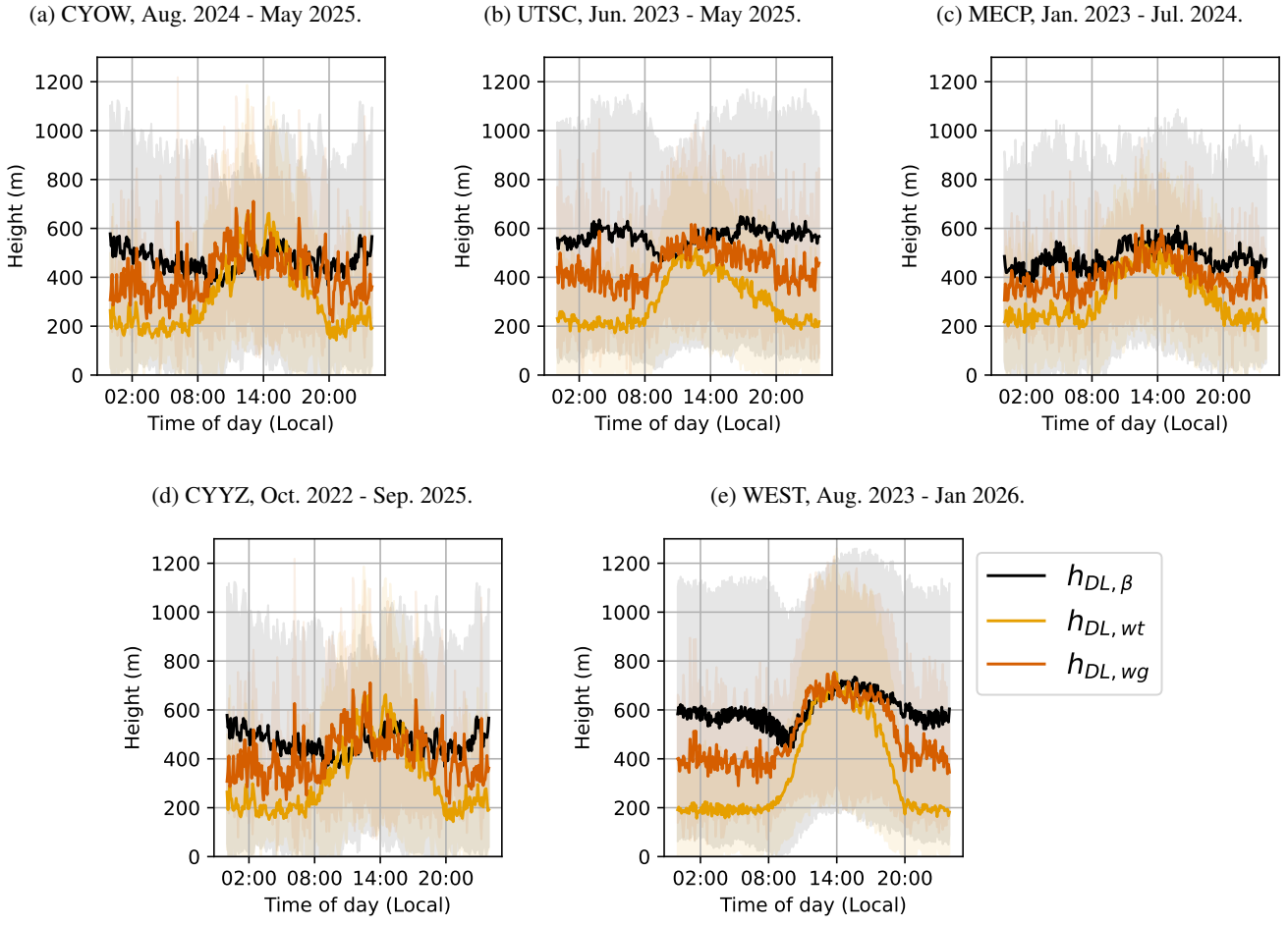


Figure 3. Diurnal means of PBLh estimates using SOLID Mesonet Doppler lidar data for all three h_{DL} algorithms at (a) CYOW, (b) UTSC, (c) MECP, (d) CYYZ, and (e) WEST to illustrate diurnal variability. $h_{DL,\beta}$ is shown in black, $h_{DL,wt}$ in yellow, and $h_{DL,wg}$ in orange, all shaded to $\pm 1\sigma$. Data collection periods for each site are listed in the captions. Note that some of the data collection periods have been limited for the purpose of this study based on data availability to minimize seasonal bias where possible.

in more stable conditions overnight) of 456 ± 443 m, as opposed to minima of 206 ± 173 m and 308 ± 113 m for $h_{DL,wt}$ and $h_{DL,wg}$, respectively.

Site-to-site, qualitative differences can be difficult to characterize due to the significantly different observation periods. CYOW and MECP have limited datasets spanning less than one year, the effect of which can be seen in the noisier mean diurnal variation seen in Figs. 3a and 3c as compared to the other sites, and their seasonal bias affects the shape of the mean diurnal variation curves across the three estimates compared to other sites. However, we can see that WEST, which does have observations spanning a full year, shows the largest diurnal amplitude. For example, $h_{DL,wt}$ has an amplitude of 598 ± 490 m at WEST, compared to 547 ± 496 m for CYYZ and 345 ± 349 m for UTSC. Additionally, while most of the sites show $h_{DL,wt}$

https://doi.org/10.5194/egusphere-2026-6344
Preprint. Discussion started: 9 November 2026
© Author(s) 2026. CC BY 4.0 License.

Table 4. Seasonal variation in each Doppler lidar estimate for sites with over a year of data availability as described by average yearly maxima, minima, and amplitudes (difference between maximum and minimum) computed from weekly means, $\pm$ 1σ in the mean. Values are presented for daytime PBLh estimates only, given that nighttime seasonal variability is limited.

Site	Estimate	Maximum (m)	Minimum (m)	Amplitude (max-min m)
	$h_{DL,\beta}$	981 $\pm$ 560	350 $\pm$ 318	631 $\pm$ 644
UTSC	$h_{DL,wt}$	666 $\pm$ 444	229 $\pm$ 141	437 $\pm$ 466
	$h_{DL,wg}$	833 $\pm$ 355	332 $\pm$ 170	501 $\pm$ 394
	$h_{DL,\beta}$	914 $\pm$ 576	338 $\pm$ 275	576 $\pm$ 638
WEST	$h_{DL,wt}$	735 $\pm$ 515	236 $\pm$ 233	499 $\pm$ 565
	$h_{DL,wg}$	1054 $\pm$ 462	341 $\pm$ 154	713 $\pm$ 487
	$h_{DL,\beta}$	763 $\pm$ 536	368 $\pm$ 336	395 $\pm$ 632
CYYZ	$h_{DL,wt}$	687 $\pm$ 483	325 $\pm$ 242	363 $\pm$ 540
	$h_{DL,wg}$	881 $\pm$ 384	356 $\pm$ 143.	525 $\pm$ 410

peaking later in the day around 14:00 with a relatively symmetric shape, a much different behaviour is exhibited at UTSC. $h_{DL,wt}$ at UTSC instead peaks earlier in the day on average (around 12:00) and follows a more gradual collapse throughout the afternoon. $h_{DL,wg}$, by contrast, behaves much the same at UTSC as at the other sites. These differences will be discussed in more detail in Section 4. In general, each of the sites appears to capture a similar diurnal evolution, with fairly consistent values between sites and similar spreads in the standard deviations in the mean of each estimate suggesting similar variability day-to-day. Nighttime values in particular are consistent between sites for each estimate.

3.1.2 Seasonal variation

The seasonal variation can be seen in Fig. 4, shown through the mean PBLh by month for the three sites that have at least one year of data (shaded to $\pm 1\sigma$). The plots are separated into "Daytime" and "Nighttime" PBLh estimates, defined in reference to sunrise and sunset times as computed for the latitude and longitude of each site by the `astral` package in Python (Kennedy), illustrating that where the height of the daytime (typically convective) PBL can change fairly dramatically with seasonal temperature fluctuations, nighttime PBL structure remains more stable. Table 4 presents yearly maxima, minima, and amplitudes computed from mean PBLh estimates for each week-of-year.

We can see that the three estimates demonstrate varying seasonal behaviour across the sites considered here. Daytime $h_{DL,\beta}$ monthly averages do not extend as low in the winter as the w-based estimates at UTSC and WEST, and $h_{DL,wt}$ does not rise as high on average during the summer as $h_{DL,wg}$ and $h_{DL,\beta}$ at all three sites. $h_{DL,wg}$ shows a larger seasonal amplitude than the other two estimates at CYYZ (525 $\pm$ 410 m vs. 395 $\pm$ 632 m for $h_{DL,\beta}$ and 363 $\pm$ 540 m for $h_{DL,wt}$) and WEST (713 $\pm$ 487 m vs. 576 $\pm$ 638 m for $h_{DL,\beta}$ and 499 $\pm$ 565 mfor $h_{DL,wt}$). At WEST (Fig. 4c), we can see this coming from a lower wintertime mean PBLh for $h_{DL,wg}$ compared to $h_{DL,\beta}$ and a higher summertime mean PBLh compared to $h_{DL,wt}$. The three estimates also generally exhibit expected behaviour, with a peak in the later, warmer summer months and declining PBLh into

https://doi.org/10.5194/egusphere-2026-6344
Preprint. Discussion started: 9 November 2026
© Author(s) 2026. CC BY 4.0 License.

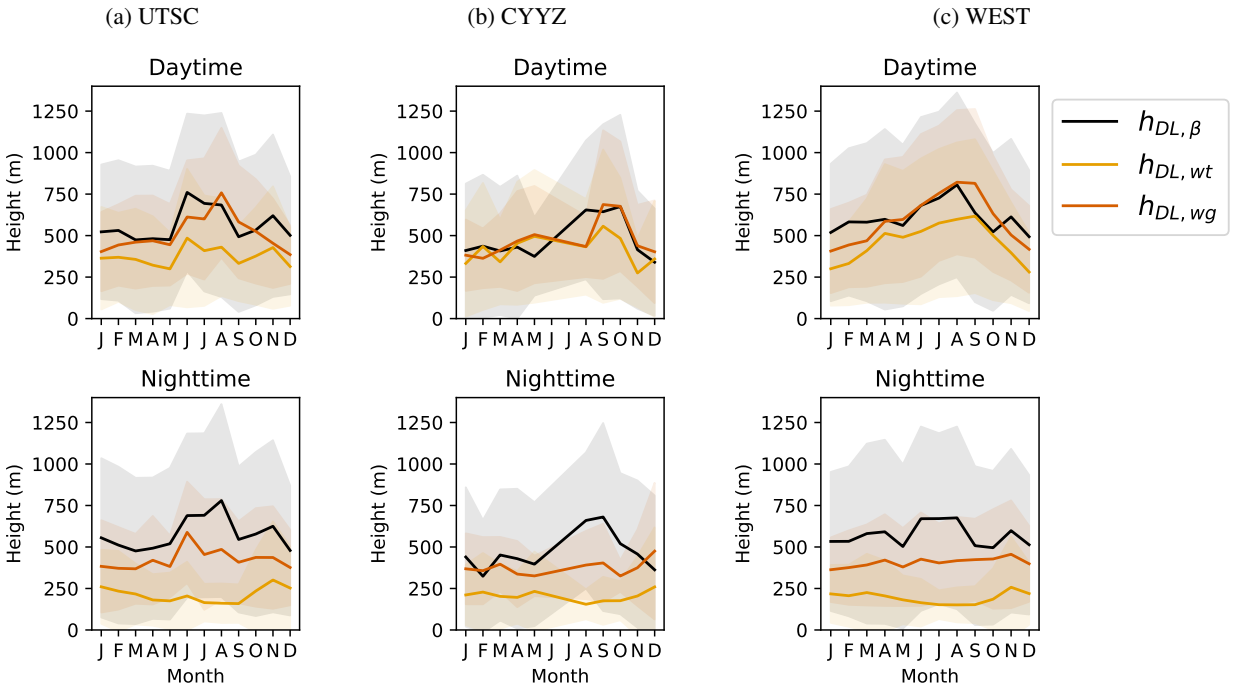


Figure 4. Seasonal variation, presented via monthly means, of PBLh estimates using SOLID Mesonet Doppler lidar data for all three algorithms for (a) UTSC, (b) CYYZ, and (c) WEST. Only these three sites are included here as the other sites do not have a sufficiently long data collection period to fully capture variation throughout the year. Top panels indicate daytime observations and bottom panels indicate nighttime observations, defined in reference to sunrise and sunset times as computed by the `astral` package in Python (Kennedy) over time for each site.

the winter. At CYYZ (Fig. 4b, all three estimates are closer together, with a less well-defined shape: all three experience peaks later on, into September and October, and do not exhibit expected rising throughout the spring and summer months. At UTSC the seasonal amplitude in $h_{DL,\beta}$ is larger (631 $\pm$ 644 m vs. 437 $\pm$ 466 m for $h_{DL,wt}$ and 501 $\pm$ 394 m for $h_{DL,wg}$), though Fig. 4a shows that $h_{DL,wg}$ exhibits more of an expected shape throughout the year, peaking in August and declining in the winter months. $h_{DL,\beta}$ and $h_{DL,wt}$, by contrast, appear to peak earlier in the year around June following a decline throughout the spring. Overnight, $h_{DL,\beta}$ monthly averages appear to remain far above the other two estimates throughout the year and $h_{DL,wg}$ similarly remains above $h_{DL,wt}$, as seen in the previous section on average throughout the dataset. There is some variation in the mean values throughout the year, though where $h_{DL,\beta}$ and $h_{DL,wg}$ generally show slightly rising nighttime PBLh in the summer, nighttime $h_{DL,wt}$ monthly means bow in the opposite direction, sinking in the summer as opposed to the winter across all three sites pictured.

The standard deviation in seasonal variations (shown in Table 4) also vary depending on time and estimation method. In Fig. 4, the spread of values (shaded) in $h_{DL,\beta}$ is much larger than for the other two estimates across all three sites, with the

https://doi.org/10.5194/egusphere-2026-6344
Preprint. Discussion started: 9 November 2026
© Author(s) 2026. CC BY 4.0 License.

spread in $h_{DL,wt}$ being the smallest overall. However, we can see that the standard deviation in each of the measures in Table 4 for $h_{DL,wg}$ is often smaller than for the other two measures, and is consistently so for the variation measure across all sites. Additionally, standard deviations in the weekly minima are consistently smaller than those of the maxima across all sites.

We can examine these seasonal impacts on the PBLh in more detail in Fig. 5, which plots the mean diurnal variation for each estimation method separated out by month, by site. Note that only the months in which observations were made are indicated for sites where the data collection period is shorter than one year. As suggested by the overall diurnal mean discussed above, $h_{DL,\beta}$ shows very little diurnal amplitude in comparison to the other two estimates throughout the year (particularly at CYYZ and WEST). These plots also confirm that the high bias exhibited by $h_{DL,\beta}$ compared to $h_{DL,wt}$ and $h_{DL,wg}$ at night persists throughout the year. The values and general shapes of the diurnal cycle are fairly consistent between $h_{DL,wt}$ and $h_{DL,wg}$ for most of the sites, though both can be seen to be highly erratic in the limited data set from CYOW and $h_{DL,wg}$ does not exhibit expected diurnal variation throughout the year at UTSC. Nighttime $h_{DL,wg}$ estimates, however, are highly variable and suffer from erratic jumps in the diurnal mean, often in the summer months, that suggest a noisier estimate. For all sites $h_{DL,wg}$ shows a high bias at night compared to $h_{DL,wt}$. Daytime $h_{DL,wg}$ estimates of the stabler, shallower winter PBLh do not appear to suffer from the same high bias as nighttime estimates compared to $h_{DL,wt}$, however, as they remain low and relatively smooth across most sites as compared to $h_{DL,wt}$ (with some erratic means in $h_{DL,wg}$ at CYOW).

When comparing site-by-site overall, we can see that the seasonal variability is most pronounced again at WEST. For example, $h_{DL,wt}$ exhibits a seasonal amplitude of 499 $\pm$ 564 m as opposed to amplitudes of 437 $\pm$ 466 m and 363 $\pm$ 540 m for UTSC and CYYZ, respectively. We can see in Fig. 4 that nighttime is comparable across all three of these sites for each estimate, whereas daytime weekly means do vary more significantly throughout the year at WEST for each estimate. Fig. 5 confirms this, showing a smaller diurnal amplitude in wintertime PBLh (as estimated by $h_{DL,wt}$) and a larger diurnal amplitude in summer PBLh at WEST compared to CYYZ and UTSC, but comparable nighttime values that remain fairly consistent throughout the year. UTSC in particular exhibits very little variation month-to-month in all estimates compared to other sites, especially for $h_{DL,wt}$, though we do see a diurnal mean that is large in amplitude in June that is consistent with the peak observed in Fig. 4a. Limited observations at CYOW produce erratic means for all estimates, though MECP observations, while limited to wintertime months, do show some of the expected variation month-to-month.

3.2 Comparing to model and reanalysis

Mean diurnal PBLh estimates for the winter period of January to March 2024 are shown in Fig. 6. The GEM PBLh estimate (referred to here as h_{GEM}) is shown in blue and the ERA5 PBLh estimate (referred to here as h_{ERA5}) is shown in green, with $h_{DL,\beta}$, $h_{DL,wt}$, and $h_{DL,wg}$ in black, yellow, and orange as before. The diurnal variability over this period for each estimate is quantified by mean daily maxima, minima, and amplitude presented in Table 5.

All estimates exhibit the diurnal cycle that we expect. However, the amplitudes of these cycles vary: h_{ERA5} and h_{GEM} diurnal means exhibit much higher peaks during the day than each of the other estimates, with mean diurnal maxima of 951 $\pm$ 487 m and 1041 $\pm$ 533 m respectively, giving respective diurnal amplitudes of 526 $\pm$ 601 m and 822 $\pm$ 608 m. $h_{DL,\beta}$, $h_{DL,wt}$, and $h_{DL,wg}$, in comparison, produce shallow daytime PBLh estimates and exhibit very limited variation throughout the day

https://doi.org/10.5194/egusphere-2026-6344
Preprint. Discussion started: 9 November 2026
© Author(s) 2026. CC BY 4.0 License.

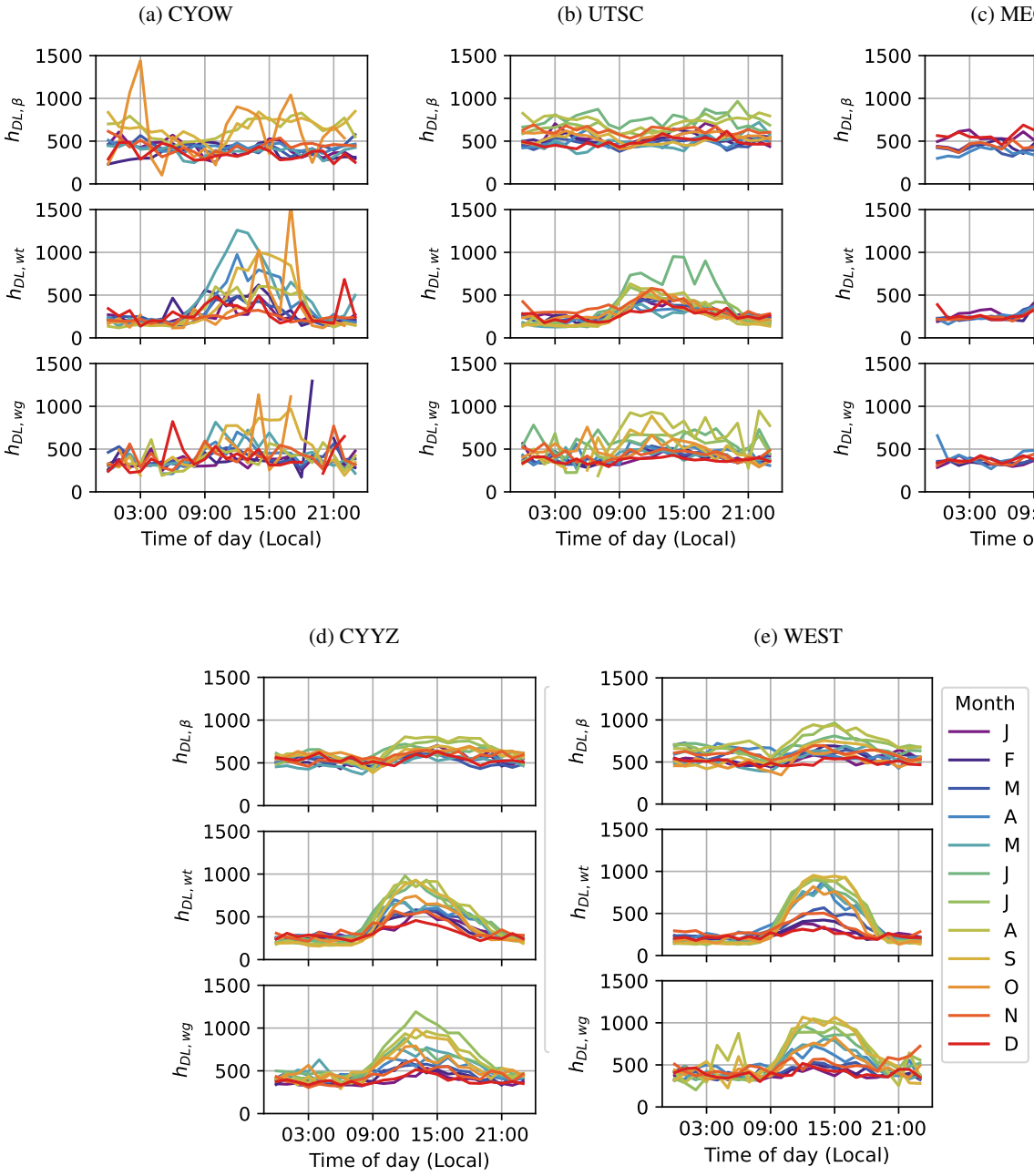


Figure 5. Diurnal means of each lidar-based PBLh estimate at (a) CYOW, (b) UTSC, (c) MECP, (d) CYYZ, and (e) WEST, separated by month of the year by colour (indicated by legend on the right) to illustrate changes in diurnal variation with the seasons. Note that CYOW and MECP do not have data available for all months in the year.

https://doi.org/10.5194/egusphere-2026-6344
Preprint. Discussion started: 9 November 2026
© Author(s) 2026. CC BY 4.0 License.

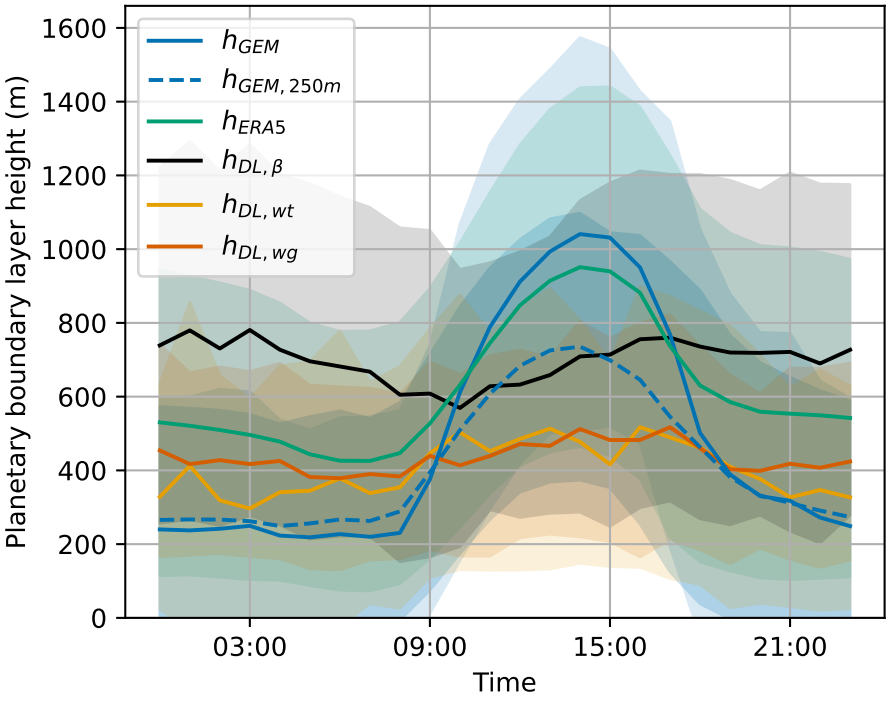


Figure 6. Diurnal means in the PBLh estimates from Doppler lidar $h_{DL,\beta}$ (black),$h_{DL,wt}$ (yellow), $h_{DL,wg}$ (orange); the estimates from GEM at 2.5 km resolution h_{GEM} (blue) and 250 m resolution $h_{GEM,250m}$ (blue, dashed); and the estimate from ERA5 h_{ERA5} (green), shaded to $\pm\sigma$. $h_{DL,x}$ have been resampled to a frequency of one hour for clarity. Computed for the Pearson Airport (CYYZ) location January to March 2024.

Table 5. Diurnal variation in PBLh estimates at the Pearson Airport site (CYYZ) over January to March 2024, as described by diurnal mean maxima, minima, and amplitudes (difference between maximum and minimum).

Estimate	Maximum (m)	Minimum (m)	Amplitude (max-min; m)
Diurnal			
$h_{DL,\beta}$	847 ± 507	548 ± 345	300 ± 613
$h_{DL,wt}$	599 ± 418	247 ± 186	352 ± 457
$h_{DL,wg}$	591 ± 291	284 ± 115	307 ± 313
h_{ERA5}	951 ± 487	426 ± 353	526 ± 601
h_{GEM}	1041 ± 533	219 ± 291	822 ± 608
$h_{GEM,250}$	741 ± 362	242 ± 275	499 ± 455

https://doi.org/10.5194/egusphere-2026-6344
Preprint. Discussion started: 9 November 2026
© Author(s) 2026. CC BY 4.0 License.

during this period: they have respective mean diurnal maximums over this period of 847 ± 507 m, 599 ± 418 m, and 307 ± 313 m, with mean respective diurnal amplitudes of 300 ± 613 m, 352 ± 457 m, and 307 ± 313 m. $h_{GEM,250M}$ similarly shows a higher daily maximum and diurnal amplitude than $h_{DL,x}$ of 741 ± 362 m and 499 ± 455 m, respectively, but we find it to be much less than its lower-resolution counterpart h_{GEM}.

Nighttime values for both h_{GEM} and $h_{GEM,250}$ are similarly relatively low in comparison to $h_{DL,x}$, with respective mean daily minima of 219 ± 291 m and 242 ± 275 m. $h_{GEM,250}$ is slightly higher on average, however, exhibiting less extreme diurnal variation. h_{ERA5}, conversely, retains a high bias at night. It follows an expected phase 3 collapse (Fig. 1) on average, but stops short of the other estimates and instead gradually lowers overnight until rising in phase 1. $h_{DL,wt}$ and $h_{DL,wg}$, with respective mean daily minima of 352 ± 457 m and 307 ± 313 m, remain below h_{ERA5} throughout the night, which has a mean daily minimum of 526 ± 601 m. $h_{DL,\beta}$, as before, does not follow the PBLh collapse into low night values due to a lack of entrainment and is not comparable.

h_{GEM}, h_{ERA5}, and $h_{GEM,250m}$ also exhibit a narrower peak in the daytime convective period (phase 2). That is, they exhibit a more abrupt collapse in the sunset period (phase 3) than the Doppler lidar-derived estimates, especially compared to $h_{DL,wg}$ which exhibits a relatively flat, consistent daytime PBLh on average. The expected slow growth of the stable nocturnal PBL (phase 4) is also not represented by any of the estimates over this period, with most (especially h_{ERA5} and $h_{DL,wg}$) actually exhibiting a decrease overnight before rising with entrainment (phase 1).

Comparison statistics between each of the estimates are presented in Table 6. These statistics show a better agreement between model estimates and $h_{DL,wt}$ than with either of the other Doppler lidar-derived estimates. For example, r is largest (indicating a stronger correlation) overall between $h_{DL,wt}$ and h_{ERA5} at $r = 0.496$, compared to the smallest magnitude correlation between $h_{DL,wg}$ and h_{GEM} of $r = 0.080$. The values presented here therefore indicate a poor correlation between all the datasets, particularly compared to values in the literature. For example, Tucker et al. (2009) find a $r = 0.91$ strength correlation between Doppler lidar and radiosonde PBLh estimates and Wang and Wang (2016) correlation strengths of over $r = 0.7$ between radiosonde-derived PBLh and reanalysis products. That is to say, there is a statistically significant difference in the PBLh variation between $h_{DL,x}$ and each of the model/reanalysis estimates. It should be noted that since these observations are taken during the winter, when there is less variability overall in the PBLh and when stable PBL conditions are more common, this is to be expected.

RMSE is similarly smallest for $h_{DL,wt}$ and $h_{GEM,250m}$ at 332 m, though bias is smallest for $h_{DL,\beta}$ and h_{ERA5} at 23 m. Daytime agreement is better than at nighttime; for example, the largest r magnitude overall is $r = 0.550$ during the daytime between $h_{DL,wt}$ and h_{ERA5}, and the smallest is at nighttime between $h_{DL,wg}$ and h_{GEM} at $r = -0.027$. The better agreement during the day is consistent with the literature (e.g. as found by Wang and Wang (2016)), as are the RMSE and bias values: RMSE and bias between Doppler lidar and aerosol lidar were found by Park et al. (2022) to be 500 m and -60 m, respectively, and similarly Schween et al. (2014) found respective RMSE and bias values of 359 m and -86 m between Doppler lidar and radiosonde estimates.

More insight can be gained from correlation plots presented in Fig. 7 (with 1:1 correlation shown for each plot by red lines, and histograms of each estimate on the diagonal). In general, the Doppler lidar-derived estimates exhibit a noisier spread

https://doi.org/10.5194/egusphere-2026-6344
Preprint. Discussion started: 9 November 2026
© Author(s) 2026. CC BY 4.0 License.

Table 6. Comparison statistics between each of the Doppler lidar-derived estimates ($h_{DL,\beta}$, $h_{DL,wt}$, $h_{DL,wg}$) and the two numerical estimates (h_{GEM}, h_{ERA5}). r is the Pearson r coefficient, RMSE is the root-mean-squared error, and bias is the mean difference in the estimates. To calculate these statistics, all estimates were resampled to an hourly sampling rate.

		h_{ERA5}			h_{GEM}			$h_{GEM,250m}$		
	Time of day	r	RMSE (m)	Bias (m)	r	RMSE (m)	Bias (m)	r	RMSE (m)	Bias (m)
$h_{DL,\beta}$	All	0.226	541	23	0.159	646	144	0.128	580	249
	Daytime	0.376	495	-116	0.318	577	-108	0.263	466	79
	Nighttime	0.133	586	169	0.067	715	428	0.084	681	430
$h_{DL,wt}$	All	0.496	399	-168	0.468	394	35	0.488	332	51
	Daytime	0.550	382	-172	0.520	387	-81	0.521	307	13
	Nighttime	0.427	412	-165	0.367	400	133	0.428	350	82
$h_{DL,wg}$	All	0.104	577	-344	0.080	567	-146	0.083	421	-64
	Daytime	0.188	587	-371	0.105	606	-298	0.177	412	-127
	Nighttime	-0.027	565	-313	-0.049	512	449	-0.068	429	7

compared to the numerical estimates than the numerical estimates to each other. A greater sensitivity to high, noisy estimates can be especially seen in the histograms of $h_{DL,wg}$ and $h_{DL,\beta}$ as compared to $h_{DL,wt}$ and the numerical estimates, as well as in their respective correlation plots. h_{ERA5} also shows a larger spread in values in the histogram than h_{GEM} or $h_{GEM,250m}$ We can also see a much lower number of data points in $h_{DL,wg}$ and, to a lesser extent, $h_{DL,wt}$ compared to the other estimates due to filtering of non-turbulent conditions and cases of non-convergence of the smoothing functions for $h_{DL,wg}$.

3.3 Case study: CYYZ February 19-20, 2024

Radiosonde-based PBLh estimates are typically considered the most reliable, and often serve as a baseline for comparison for PBLh estimation methods. There is, unfortunately, no regular radiosonde launch within Southern Ontario to provide a direct comparison for PBLh estimates from the SOLID Mesonet. As an approximation, we instead make use of the NOAA radiosonde launches at the Greater Buffalo International Airport (Station 72528; latitude 42.940 °N, longitude 78.725 °W; NOAA (2026)). We compare PBLh estimates from the radiosonde data collected to those from measurements taken at the CYYZ site, which is the closest of the SOLID Mesonet sites. In an attempt to ensure similar PBL structure between the two locations, we use weather maps to select days with high-pressure systems and relatively homogenous atmospheric conditions between CYYZ and Buffalo International Airport. The radiosonde launches occur at 00:00 and 12:00 UTC daily, which corresponds to a local time of 19:00 and 07:00 EST. We have therefore chosen a case study the period of 19:00 EST February 19th to 19:00 EST February 20th, 2024, for overlap with the SWAPIT data collection period, to investigate $h_{DL,x}$ in more detail and compare to radiosonde-based estimates.

https://doi.org/10.5194/egusphere-2026-6344
Preprint. Discussion started: 9 November 2026
© Author(s) 2026. CC BY 4.0 License.

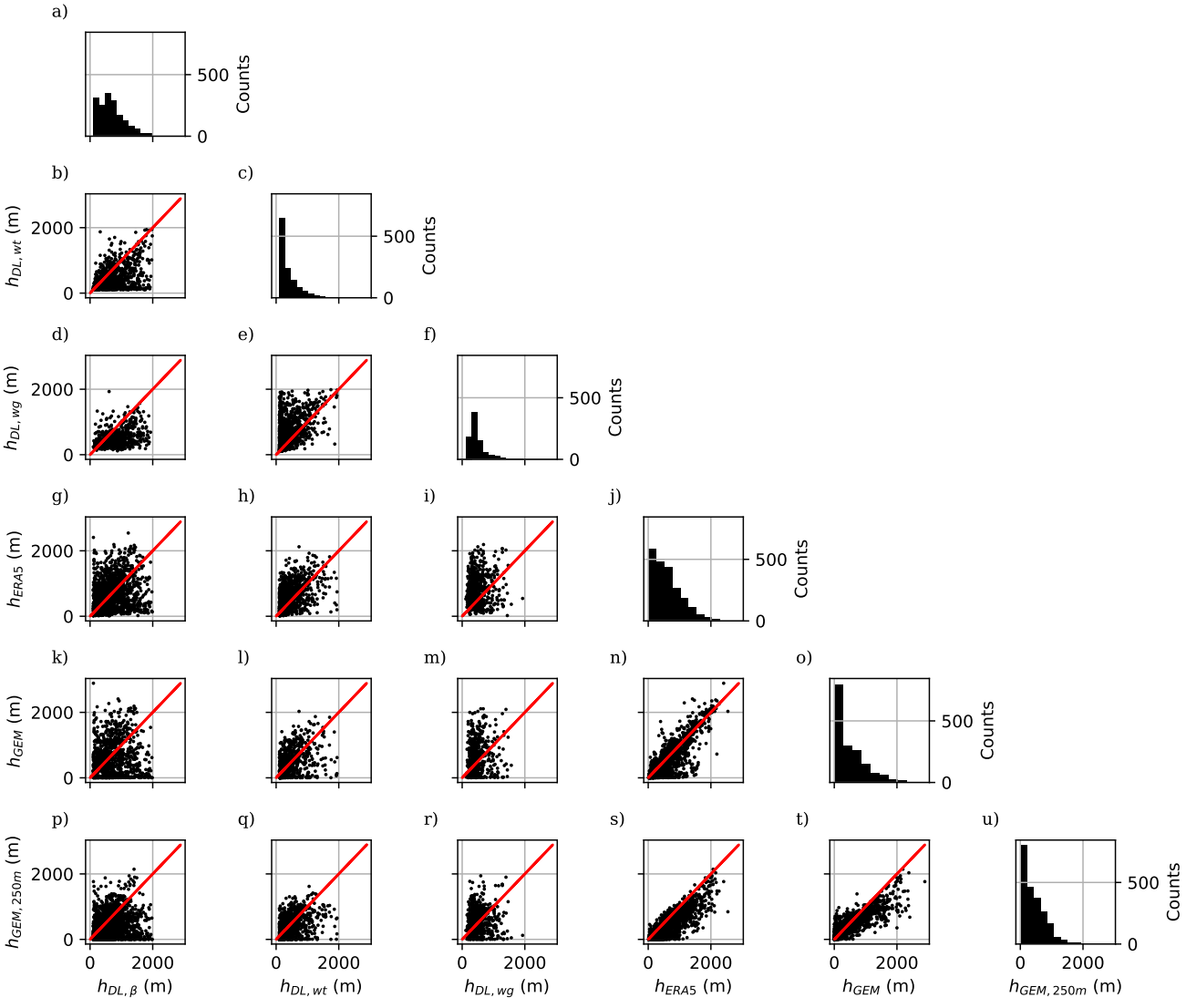


Figure 7. Correlation plots between each of the PBLh estimation methods (with histograms of each on the diagonal) for CYYZ over January to March 2024: a) a histogram of $h_{DL,\beta}$, b) $h_{DL,wt}$ vs. $h_{DL,\beta}$, c) a histogram of $h_{DL,wt}$, d) $h_{DL,wg}$ vs. $h_{DL,\beta}$, e) $h_{DL,wg}$ vs. $h_{DL,wt}$, f) a histogram of $h_{DL,wg}$, g) h_{ERA5} vs. $h_{DL,\beta}$, h) h_{ERA5} vs. $h_{DL,wt}$, i) h_{ERA5} vs. $h_{DL,wg}$, j) a histogram of h_{ERA5}, k) h_{GEM} vs. $h_{DL,\beta}$, l) h_{GEM} vs. $h_{DL,wt}$, m) h_{GEM} vs. $h_{DL,wg}$, n) h_{GEM} vs. h_{ERA5}, o) a histogram of h_{GEM}, p) $h_{GEM,250m}$ vs. $h_{DL,\beta}$, q) $h_{GEM,250m}$ vs. $h_{DL,wt}$, r) $h_{GEM,250m}$ vs. $h_{DL,wg}$, s) $h_{GEM,250m}$ vs. h_{ERA5}, t) $h_{GEM,250m}$ vs. h_{GEM}, u) a histogram of $h_{GEM,250m}$. The linear relationship with slope 1 is shown in red on each plot.

https://doi.org/10.5194/egusphere-2026-6344
Preprint. Discussion started: 9 November 2026
© Author(s) 2026. CC BY 4.0 License.

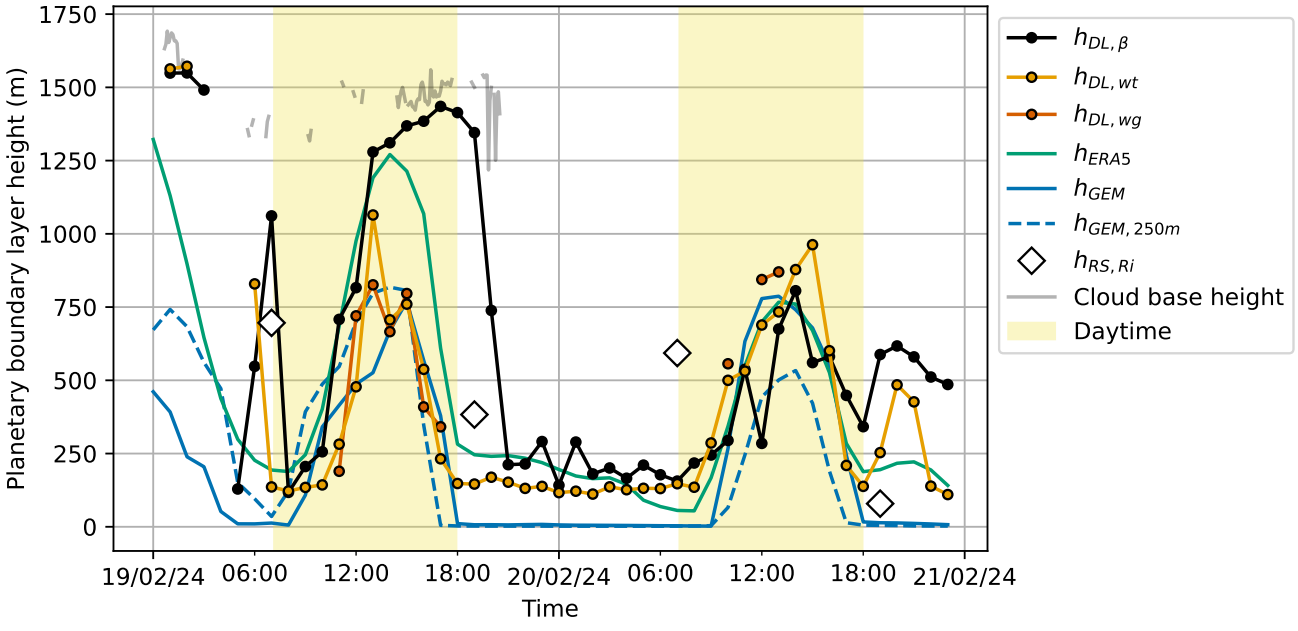


Figure 8. PBLh estimates from Doppler lidar ($h_{DL,\beta}$,$h_{DL,wt}$, $h_{DL,wg}$), GEM (h_{GEM}), ERA5 (h_{ERA5})), and Buffalo Airport radiosonde $h_{RS}$for the case study period of February 19th-20th, 2024. For clarity, each of $h_{DL,x}$ has been resampled to an hourly frequency. Daytime (between sunrise and sunset as calculated by the `astral` Python package) is indicated with yellow shading.

There are a number of possible methods for the estimation of PBLh from radiosonde measurements. In this study we use the height of the critical bulk Richardson number as is used by ERA5 to estimate PBLh ($h_{RS,Ri}$), described above, for consistency. Surface values for the inputs to Eq. 2.4.2 are taken from weather data collected at Buffalo Airport (Meteostat, 2026).

PBLh estimates for each of the Doppler lidar, model, and radiosonde methods are plotted for the case study time period in Fig. 8. Daytime, the period between the sunrise and sunset times, is indicated with pale yellow shading. Cloud base height is also shown for reference with a grey line. For clarity, the Doppler lidar methods $h_{DL,x}$ have been resampled to hourly observations.

Due to the variability in PBLh estimates even between different methods using radiosonde measurements, it is not possible to treat $h_{RS,Ri}$ as a baseline to compare $h_{DL,x}$ to. We can, however, note that the generally good agreement between $h_{DL,x}$ and $h_{RS,Ri}$ as seen in Fig. 8, even across the distance between CYYZ and the Buffalo International Airport site, suggests robustness in $h_{DL,x}$. Otherwise, we can draw further observations from the behaviour of each of the estimates presented here over the case study period. $h_{DL,\beta}$ can be seen to tend towards heights that are coincident with cloud base heights in adjacent cloudy observations (even in the observations considered here, which have been limited to clear-sky points). While sometimes PBLh can coincide with cloud base height as warmer, humid air cools rapidly from mixing with entrained free atmosphere air, it is not always the case that the PBL extends up to the cloud base height (Stull, 2012). $h_{DL,\beta}$ does show some ability to follow

https://doi.org/10.5194/egusphere-2026-6344
Preprint. Discussion started: 9 November 2026
© Author(s) 2026. CC BY 4.0 License.

a shallower, more stable PBLh later in the night between February 19th and 20th, suggesting the presence of some, if weak, convection. $h_{DL,wt}$ similarly tracks the nighttime PBLh well during this period. Given that we only compute $h_{DL,wt}$ in the presence of turbulence ($\sigma_w^2 > 0.04\ \mathrm{m}^2/\mathrm{s}^2$ at the surface), this confirms weakly convective nighttime conditions. $h_{DL,wt}$ can be seen to track diurnal PBLh evolution reasonably well as compared to theoretical expectations (Fig. 1). The points at which $h_{DL,wg}$ produces an estimate are consistent with $h_{DL,wt}$. However, it suffers from frequent data gaps where σ_w^2 observations were clearly too sparse or noisy for fitting a smoothing function, as required for identifying minima in the gradient.

As with the diurnal means presented in Fig. 6, we can see a high bias during the day on February 19th in h_{ERA5} compared to $h_{DL,x}$ and a better agreement between $h_{DL,x}$ and the GEM estimates. On February 20th, however, h_{ERA5}, h_{GEM}, and $h_{DL,x}$ are in good agreement, reaching higher during the day, and $h_{GEM,250m}$ remains lower down. Overnight across both days, it can be seen that h_{GEM} and $h_{GEM,250m}$ sink all the way to the surface where h_{ERA5} and $h_{DL,x}$ remain aloft. It should be noted that $h_{DL,x}$ all have an imposed minimum of 100 m as opposed to GEM's minimum of 30 m, but most data points over this period put $h_{DL,x}$ over this minimum, if slightly. Even with these differences, it can be seen that all of these estimates generally follow a similar evolution in the PBLh throughout the two days considered here.

4 Discussion

The w-based methods qualitatively and quantitatively capture the general shape of the expected variations in PBLh diurnally and seasonally across all five sites considered in this study. Both $h_{DL,wt}$ and $h_{DL,wg}$ reproduce the expected phases in Fig. 1, aside from a lack of growth overnight in the nocturnal PBL (during the case study period and on average). This failure to track overnight PBL growth is attributable to the inability of $h_{DL,wt}$ and $h_{DL,wg}$ to identify the stable PBLh, therefore biasing nighttime estimates towards weakly or neutrally stable conditions that experience less radiative cooling from the surface and so do not grow in strength overnight as the stable PBL does.

The tendency of $h_{DL,wt}$ and $h_{DL,wg}$ to agree well with each other in the daytime on average and during the case study period suggests that both methods function well in convective conditions. Overnight, we find that the high bias of mean diurnal values of $h_{DL,wg}$ compared to $h_{DL,wt}$ occurs due to a tendency in $h_{DL,wg}$ to produce a more variable estimate, rather than a systemic bias between the two. Measurement noise can often create large, sharp gradients, so overnight $h_{DL,wg}$ is often characterized by large jumps to high values in PBLh, where Doppler lidar signal is poor. When the estimates are averaged across all days, then, we see a high bias in the $h_{DL,wg}$ mean overnight compared to $h_{DL,wt}$ across all sites (Fig. 3). Given the ability of $h_{DL,wg}$ to otherwise capture the expected diurnal evolution in the PBLh and agree well with $h_{DL,wt}$, further refining the method to reduce the sensitivity to noise could make it an effective location-agnostic estimate, as opposed to $h_{DL,wt}$ which depends on choice of threshold. This could be potentially accomplished by refining the noise-reduction QC methods applied to the data, improving smoothing procedures applied to $\nabla\sigma_w^2$, or applying the Haar wavelet method often used for aerosol backscatter PBLh estimation methods (Tucker et al., 2009; Aliabadi et al., 2016) to identify sharp dropoffs in $\nabla\sigma_w^2$ more systematically. In its current form, however, $h_{DL,wg}$ is less reliable overnight.

https://doi.org/10.5194/egusphere-2026-6344
Preprint. Discussion started: 9 November 2026
© Author(s) 2026. CC BY 4.0 License.

$h_{DL,\beta}$, conversely, struggles to capture both the appropriate diurnal and seasonal variations. During the day, diurnal means across all sites are roughly consistent with the w-based estimates and successfully track the evolution of the convective PBLh. This is useful as a test of robustness for all three estimates: where $h_{DL,wt}$ and $h_{DL,wg}$ estimate the PBLh following the assumption that σ_w experiences a sharp dropoff at the PBLh characteristic of the transition between a turbulent PBL and a stable free atmosphere, $h_{DL,\beta}$ instead identifies it as the middle of the entrainment zone by tracking the process of entrainment itself. A good agreement between all of $h_{DL,x}$ during daytime convective conditions, despite using slightly different theoretical approaches and observations of different atmospheric components, increases confidence in the estimates in the case of convectively unstable PBLh. $h_{DL,\beta}$ has also been found in other studies to be generally reliable in convective conditions as compared to other lidar methods and radiosonde observations (Hennemuth and Lammert, 2006; Lammert and Bösenberg, 2006; Caicedo et al., 2017).

Overnight, however, as well as in colder wintertime conditions, $h_{DL,\beta}$ fails to capture the evolution of the stable or neutrally stable PBLh. In these cases, the entrainment zone assumption typically fails, as the processes that cause entrainment stop with the collapse of the convective PBL. $h_{DL,\beta}$ then instead tracks noise or other processes causing variance in aerosol concentration (like cloud formation), seen across all sites by its comparatively high nighttime/minimum values in the diurnal means in Fig. 3 and Table 3, lower seasonal variation amplitude in Fig. 4 and Table 4, and higher standard deviation at nighttime in both. We can see in the case study (Fig. 8) that there are cases like the night between February 19th and 20th, 2024, where enough weak convection occurs during the night for $h_{DL,\beta}$ to estimate a PBLh consistent with $h_{DL,wt}$, but that biases in the diurnal and seasonal mean $h_{DL,\beta}$ show that these conditions do not occur often enough for $h_{DL,\beta}$ to be considered reliable for the non-unstable PBL. Additionally, we see in the case study that in the presence of clouds, $h_{DL,\beta}$ may tend towards estimating the PBLh to be coincident with the cloud layer rather than agreeing with $h_{DL,wt}$ and $h_{DL,wg}$. This possibly indicates the presence of a multi-layered structure (Johansson et al., 2005; Hennemuth and Lammert, 2006), where lofted aerosol layers can cause $h_{DL,\beta}$ to mistakenly select higher altitudes with maximized σ_β^2 as the PBLh (Caicedo et al., 2017).

Site-to-site, there are some differences in the variability of $h_{DL,wt}$. For example, MECP and UTSC have a much lower diurnal variation in $h_{DL,wt}$ than the other sites. This could be attributable to physical differences across the sites or seasonal biases introduced by data sampling: the disparity is mirrored by $h_{DL,wg}$, suggesting that it is not caused by an issue in $h_{DL,wt}$ site-to-site. As shown in Fig. 2, UTSC has more data availability during winter months (which exhibit lower PBLh and less variability throughout the day), as does MECP to a lesser extent. CYOW, however, similarly has data availability limited to winter months, but does not exhibit this decrease in variability in $h_{DL,wt}$ and $h_{DL,wg}$ compared to other sites. Further investigation into the viability of the chosen threshold value ($\sigma_w^2 = 0.04\ \mathrm{m^2/s^2}$) for $h_{DL,wt}$ would clarify some of these differences (even for $h_{DL,wg}$, as the threshold is used to discard data with non-turbulent conditions), and will be performed prior to the operational implementation of $h_{DL,wt}$ for making PBLh estimates available with SOLID Mesonet data for forecasters. Some differences between sites can be interpreted to be physical: for example, afternoon values in $h_{DL,wt}$ and $h_{DL,wg}$ sink lower earlier for CYYZ and UTSC, which are closer in proximity to Lake Ontario, than for WEST, which exhibits more of a consistent, plateau-like shape during the day. WEST also generally exhibits a larger diurnal and seasonal variation across all estimates than at the other sites. These differences could be partially attributed to the moderating lake effect, as discussed

https://doi.org/10.5194/egusphere-2026-6344
Preprint. Discussion started: 9 November 2026
© Author(s) 2026. CC BY 4.0 License.



further in Appendix A. However, as WEST is the only rural site in the SOLID Mesonet, this could also have implications for the differences in convective PBL growth in farmland regions vs. urban/suburban environments.

Comparison to the model and reanalysis estimates h_{GEM}, $h_{GEM,250m}$, and h_{ERA5}, as in Fig. 6, suggests that each estimate tracks the phases of the expected diurnal variation at approximately the same times of day on average. However, there are some differences. For example, h_{ERA5} exhibits a similar high bias overnight to $h_{DL,wg}$. The diurnal mean for h_{ERA5} is not biased by individual noisy estimates but by a systemic high bias compared to $h_{DL,x}$ throughout the dataset, clearly applying to the daytime as well. Since $h_{RS,Ri}$, which uses the same methodology as h_{ERA5}, does not exhibit as consistent a bias, it is possible that the high bias is not due to the choice of critical bulk Richardson number ($Ri_b = 0.25$) threshold but rather related to the input variables of ERA5 and/or its resolution. The choice of threshold can be further tested in future to confirm this. Similarly, h_{GEM}'s tendency towards a high bias in PBLh during the day and low bias at night compared to the other datasets, especially considering the nighttime behaviour during the case study period of h_{GEM} tending towards estimating PBLh to be at the surface, suggests a possible systemic underestimation of PBLh in the stable case. This could translate to poor estimation of surface pollution, as found by Zhao et al. (2019) (in contrast to ERA5, for example, which can be seen to perform better in this context in Zhao et al., 2024). However, the better agreement on average between $h_{GEM,250m}$ and $h_{DL,x}$ suggests that higher model resolution, especially in environments as complex as that of the urban, near-lake CYYZ site, could produce a more reliable PBLh estimate. This result is consistent with prior literature on the subject (e.g. Leroyer et al., 2014). We can see that this better agreement is not constant, however, with the low bias in $h_{GEM,250m}$ on the second case study day. The tendency of h_{ERA5}, h_{GEM}, and $h_{GEM,250m}$ to rise faster and collapse earlier, exhibiting a narrower peak in PBLh during the day, has also been observed in other models, attributable to model error (Hegarty et al., 2018; Park et al., 2022).

5 Conclusions

This study presented three methods for the estimation of the PBLh from Doppler lidar observations of aerosol backscatter β and vertical wind speed w collected by the SOLID Mesonet: $h_{DL,\beta}$, tracking the centre of the entrainment zone as an estimate of the PBLh; $h_{DL,wt}$, identifying the PBLh as the height of a decrease in vertical wind speed variance below a prescribed threshold; and $h_{DL,wg}$, setting the PBLh to be the height at which the vertical wind speed variance drops sharply, identified by a large negative gradient.

As a general assessment, while the w-based estimates are fairly consistent with each other, $h_{DL,wg}$ can be considered less reliable due to its tendency towards highly variable estimates as caused by measurement noise, even after quality control measures are applied. This causes a high bias in $h_{DL,wg}$ compared to $h_{DL,wt}$ in any average measure of the PBLh variability for that method. The bias is especially evident in nighttime stable nocturnal PBL conditions as the Doppler lidar range becomes especially limited, suggesting that $h_{DL,wg}$ is particularly unreliable at night. $h_{DL,wg}$ also suffers from a dependence on the smoothing function applied prior to computing the gradient, causing data gaps for measurements for which a smoothing function fit cannot converge. $h_{DL,\beta}$, while showing consistency with the other two estimates during daytime convective conditions, fails completely to track expected afternoon (phase 3) PBLh collapse and nighttime nocturnal stable PBLh due to the failure of

https://doi.org/10.5194/egusphere-2026-6344
Preprint. Discussion started: 9 November 2026
© Author(s) 2026. CC BY 4.0 License.

the entrainment assumption. It also struggles with tracking seasonal variation into the wintertime months for the same reasons. $h_{DL,wt}$ qualitatively exhibits expected diurnal and seasonal variations, and shows good agreement with model and radiosonde PBLh estimates. Despite its dependence on the choice of threshold, it also does not exhibit any large discrepancies location-to-location that are not also tracked by the other two estimates. Thus, the most reliable estimate for usage with data collected by the SOLID Mesonet at this time was found to be $h_{DL,wt}$.

Comparisons of these estimates to PBLh outputs from GEM (at both 2.5 km and 250 m resolution), ERA5, and radiosonde estimates both affirm the soundness of the Doppler lidar-derived estimates and show the potential to use them in conjunction with atmospheric composition observations to assess the performance. In the diurnal mean over January-March 2024 and in the case study of February 19th-20th 2024, we see a general agreement in the shape of diurnal evolution in PBLh between all estimates. However, h_{ERA5}, h_{GEM}, and $h_{GEM,250m}$ are all seen to exhibit a systemic high daytime bias on average and narrower peak than $h_{DL,x}$. h_{GEM} also shows a low bias overnight compared to $h_{DL,x}$, even tending towards the surface in the case study, whereas h_{ERA5} maintains a high bias overnight, indicating that investigation of the algorithm used in GEM, and in particular for more stable conditions, is necessary. $h_{GEM,250m}$ shows a better agreement with $h_{DL,x}$, with lower daytime values, higher overnight values, and more gradual collapse in the afternoon on average (though it still exhibits the same biases as h_{GEM} to a smaller degree). These conclusions suggest the possibility that a higher model resolution and/or adjustment to model PBLh estimation algorithms could improve the parametrization of mixing processes for numerical weather prediction.

Aside from continuing to improve the reliablility of the estimates presented here, future work will use Doppler lidar-derived PBLh estimates to improve our understanding of the interplay between PBLh evolution and atmospheric pollutants in the PBL and surface layer. For example, as discussed in previous sections, some models show a tendency towards over-prediction of surface pollutants that may be influenced by discrepancies in PBLh estimation. These discrepancies could improved through assimilation of PBLh observation datasets as has been performed in some studies (Tangborn et al., 2021; Pan et al., 2025). However, there also exists a disparity in the fundamental theoretical assumptions between various definitions of the PBLh used across observational and modelling techniques, particularly that of the difference between the turbulence-informed definition used here and that of the mixed layer often used when observing the evolution of pollutant distributions. We can further use long-term Doppler-lidar PBLh observations to better understand this issue and improve consistency in observations and models.

Future work will continue to improve on the Doppler-lidar PBLh estimates presented here. For example, possible improvements to the noise sensitivity inherent in $h_{DL,wg}$ will be tested, such as refining noise filtering procedures and applying a Haar wavelet method to identify sharp decreases in $\nabla\sigma_w^2$. Threshold-dependency in $h_{DL,wt}$ will also be investigated in more detail, and any need for changes in the threshold value between SOLID Mesonet sites identified. Additional possibilities for future work in refining the estimates presented here include integrating site-to-site homogenization as performed by Wang and Wang (2016), pairing temperature inversion measurements from the co-located Microwave Radiometer instrument at CYOW for stable PBLh detection (de Arruda Moreira et al., 2018), and investigating the impact of including cloudy conditions in the dataset. These PBLh estimates will also be used to aid in interpreting air quality observations made over the SWAPIT campaign, providing insight into urban wintertime air quality modelling and the impact of PBLh evolution on the diurnal variability of atmospheric constituents.

https://doi.org/10.5194/egusphere-2026-6344
Preprint. Discussion started: 9 November 2026
© Author(s) 2026. CC BY 4.0 License.

Appendix A: ERA5 sub-grid interpolation

Given that the numerical outputs we integrate from ERA5 are obtained from a grid with a resolution of 31 km (0.25°), we apply interpolation schemes for comparison to PBLh estimates at SOLID Mesonet sites. In particular, differences in the PBLh at the sites can be quite pronounced with differing proximity to Lake Ontario: the planetary boundary layer height is generally lower over and near lakes due to increased stratification (Ma et al., 2026). Influence of marine air on the boundary layer has been studied in cities such as Chicago (Jackson et al., 2025), and Sao Paulo (Riberio et al., 2018). In Chicago, from measurements taken throughout July 2024, a three-layered structure was observed under the influence of a lake breeze: the lowest sea-breeze layer, followed by a stable residual layer, and topped by another residual layer with eastward flow. In Sao Paulo, the PBLh was found to decrease in the presence of coastal marine air, through creation of a thermal internal boundary layer, similar to the results from (Jackson et al., 2025).

We observe a similar pattern, as shown in Fig. A1, over Southwestern Ontario. Looking at the median of observations taken in the month of July between 2022-2024 (Fig. A1a), we can see the lowest afternoon PBLh values over Lake Ontario and notably shallower PBL along the shorelines compared to inland. Note that in January (Fig. A1b), the conditions are similarly affected but inverted: the moderating effect of the lake now warms the air compared to inland. In order to account for this lake effect and ensure comparisons are appropriate, we interpolate hourly PBLh estimates from the ERA5 standard grid to the precise latitude and longitude of the CYYZ (43.6660°, -79.6062°). Two methods were employed for interpolation: 1) An inverse distance-weighted (IDW) interpolation to CYYZ, where distances are computed to the nearest four grids, and 2) a weighted-mean of surrounding grid cells, based on the percentage of grid-cells in a defined box (bounds 43.54° $\leq$ Latitude $\leq$ 43.78°, and -79.85° $\leq$ Longitude $\leq$ -79.35°) around Pearson. The diurnal mean of the resultant interpolated ERA5 PBLh estimates h_{ERA5} are shown in A2. To quantify the marine-air effect, we also show h_{ERA5} at the grid point 43.75°, -79.75° containing CYYZ, and perform another IDW interpolation to the point 43.65°, -79.39° (Downtown Toronto).

The lake effect is apparent, with the highest and lowest afternoon heights occurring at the point 43.75 °N, 79.65 °W (furthest away from Lake Ontario), and downtown Toronto (more exposed to Lake Ontario than CYYZ), respectively, as expected given Fig. A1. Results from the IDW and box interpolation were nearly identical, where the absolute value of the mean difference was only 1.5 meters. As a result, we use an IDW interpolation for our comparison estimates for consistency with ERA5, for which this method is used when re-gridding data.

https://doi.org/10.5194/egusphere-2026-6344
Preprint. Discussion started: 9 November 2026
© Author(s) 2026. CC BY 4.0 License.

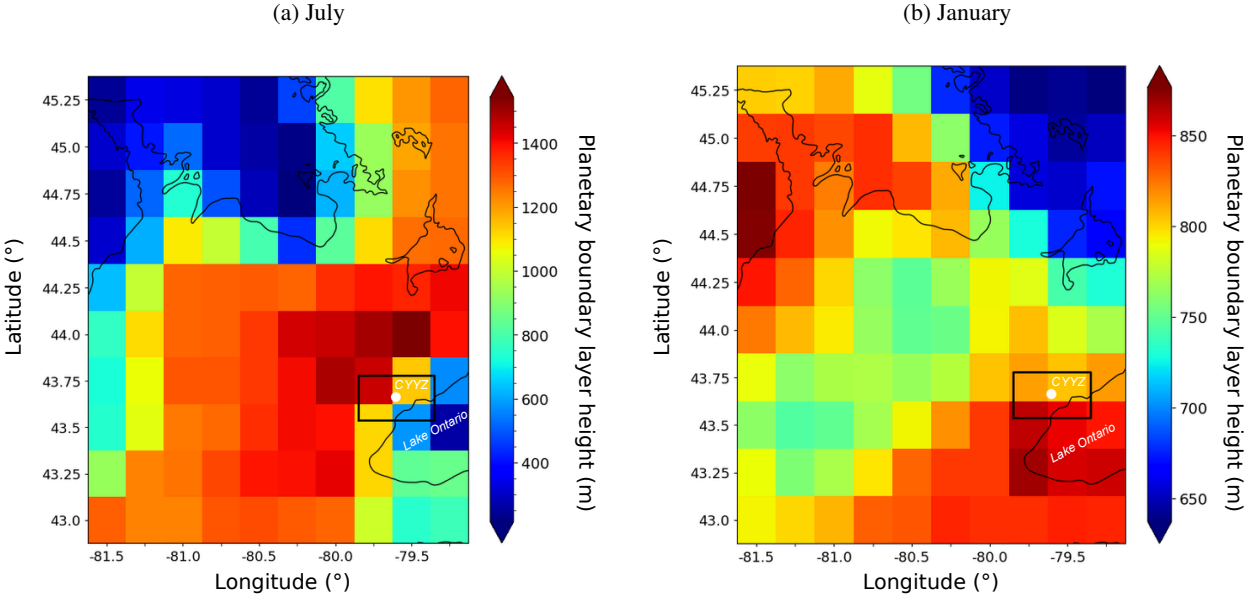


Figure A1. Median PBLh for afternoon hours (12 to 17 local time) over the months of a) July and b) January 2022-2025. The white dot indicates the location of interpolation (43.6660°N, 79.6062°W, corresponding to CYYZ). The outline of the box used in the box interpolation method is also displayed.

https://doi.org/10.5194/egusphere-2026-6344
Preprint. Discussion started: 9 November 2026
© Author(s) 2026. CC BY 4.0 License.

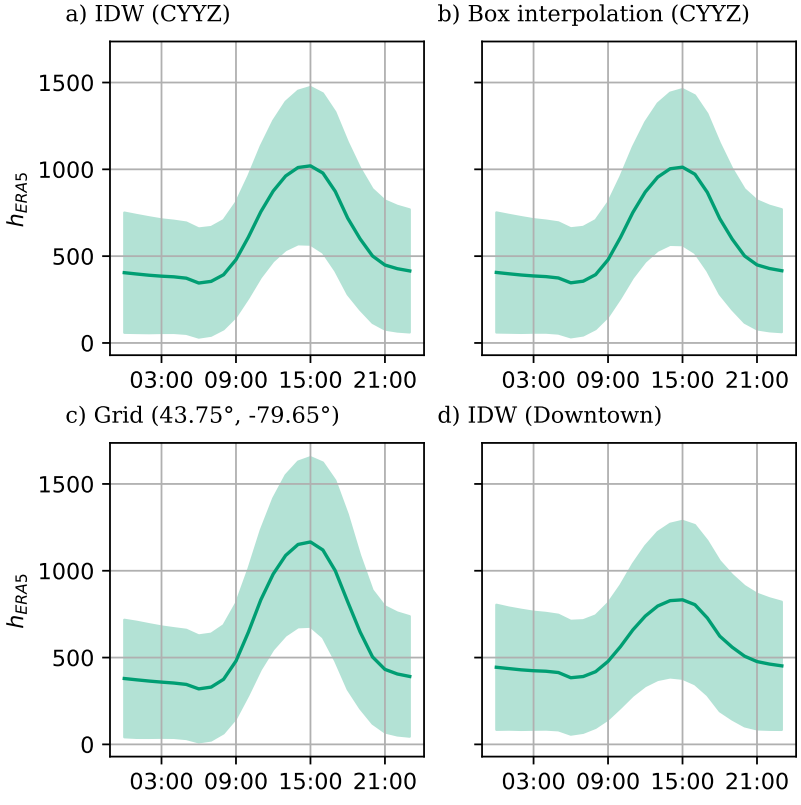


Figure A2. Diurnal mean of h_{ERA5} over the period of October 2022 to September 2025 illustrating varying interpolation schemes: a) IDW interpolation to CYYZ (43.6660°N, 79.6062°W), b) box interpolation to CYYZ, c) the grid point (43.75°, -79.75°), and d) IDW interpolation to downtown Toronto (43.65°N, 79.39°W). Shaded to $\pm 1\sigma$.

https://doi.org/10.5194/egusphere-2026-6344
Preprint. Discussion started: 9 November 2026
© Author(s) 2026. CC BY 4.0 License.

Code and data availability. This project used data from the Southern Ontario LIDar Mesonet, available at http://hiwr.ca/mesonet.php (Mariani et al., 2026), the Global Environment Multiscale model (Côté et al., 1998; McTaggart-Cowan et al., 2019), and the ECMWF ERA5 Reanalysis available at https://cds.climate.copernicus.eu/datasets/reanalysis-era5-single-levels (Hersbach et al., 2020) It also used data from Buffalo International Airport: radiosonde data available at https://weather.uwyo.edu/upperair/sounding.shtml (NOAA, 2026), and weather data available at https://meteostat.net/en/station/72528 (Meteostat, 2026). Replication data are available at https://doi.org/10.5683/SP4/N63T8Y (Duff et al., 2026).

Author contributions. ZM and EG conceived this project. PD was responsible for conducting the data analysis, creating all the figures and plots, and drafting the paper. SS conducted the interpolation analysis and drafted the corresponding section. ZM, EG, and KS provided significant input throughout the study, and ZM, EG, SL, MG, and KS provided significant edits to the paper. SL and AL provided GEM data products and significant computational and theoretical background support throughout the study. RC provided the processed SOLID Mesonet Doppler lidar data product. All coauthors provided feedback on the paper.

Competing interests. At least one of the authors is a member of the editorial board of Atmospheric Measurement Techniques.

Acknowledgements. This work was funded under the Study of Winter Air Pollution in Toronto (SWAPIT) through the Air Pollution program at Environment and Climate Change Canada (ECCC). Thank you to Robert Reed and Stephen Holden (ECCC) for deploying and maintaining the Doppler lidars, and Ayrton Zadra for his internal documentation on the GEM algorithm for PBLh estimation.

https://doi.org/10.5194/egusphere-2026-6344
Preprint. Discussion started: 9 November 2026
© Author(s) 2026. CC BY 4.0 License.

References

Aliabadi, A., Staebler, R., De Grandpré, J., Zadra, A., and Vaillancourt, P.: Comparison of estimated atmospheric boundary layer mixing height in the Arctic and southern Great Plains under statically stable conditions: experimental and numerical aspects, Atmosphere-Ocean, 54, 60–74, https://doi.org/10.1080/07055900.2015.1119100, 2016.

Anderson, P. and Neff, W.: Boundary layer physics over snow and ice, Atmospheric Chemistry and Physics, 8, 3563–3582, https://doi.org/10.5194/acp-8-3563-2008, 2008.

Balsley, B., Frehlich, R., Jensen, M., and Meillier, Y.: High-resolution in situ profiling through the stable boundary layer: Examination of the SBL top in terms of minimum shear, maximum stratification, and turbulence decrease, Journal of the Atmospheric Sciences, 63, 1291–1307, https://doi.org/10.1175/JAS3671.1, 2006.

Barlow, J. F., Halios, C. H., Lane, S., and Wood, C. R.: Observations of urban boundary layer structure during a strong urban heat island event, Environmental Fluid Mechanics, 15, 373–398, https://doi.org/10.1007/s10652-014-9335-6, 2015.

Belmonte, A. and Rye, B. J.: Heterodyne lidar returns in the turbulent atmosphere: performance evaluation of simulated systems, Applied Optics, 39, 2401–2411, https://doi.org/10.1364/AO.39.002401, 2000.

Beyrich, F.: Mixing height estimation from sodar data—a critical discussion, Atmospheric Environment, 31, 3941–3953, https://doi.org/10.1016/S1352-2310(97)00231-8, 1997.

Caicedo, V., Rappenglück, B., Lefer, B., Morris, G., Toledo, D., and Delgado, R.: Comparison of aerosol lidar retrieval methods for boundary layer height detection using ceilometer aerosol backscatter data, Atmospheric Measurement Techniques, 10, 1609–1622, https://doi.org/10.5194/amt-10-1609-2017, 2017.

Cohn, S. A. and Angevine, W. M.: Boundary Layer Height and Entrainment Zone Thickness Measured by Lidars and Wind-Profiling Radars, Journal of Applied Meteorology, 39, 1233 – 1247, https://doi.org/10.1175/1520-0450(2000)039<1233:BLHAEZ>2.0.CO;2, 2000.

Côté, J., Gravel, S., Méthot, A., Patoine, A., Roch, M., and Staniforth, A.: The operational CMC–MRB global environmental multiscale (GEM) model. Part I: Design considerations and formulation, Monthly Weather Review, 126, 1373–1395, https://doi.org/10.1175/1520-0493(1998)126<1373:TOCMGE>2.0.CO;2, 1998.

Davies, F., Middleton, D., and Bozier, K.: Urban air pollution modelling and measurements of boundary layer height, Atmospheric Environment, 41, 4040–4049, https://doi.org/10.1016/j.atmosenv.2007.01.015, 2007.

de Arruda Moreira, G., Guerrero-Rascado, J. L., Bravo-Aranda, J. A., Benavent-Oltra, J. A., Ortiz-Amezcua, P., Róman, R., Bedoya-Velásquez, A. E., Landulfo, E., and Alados-Arboledas, L.: Study of the planetary boundary layer by microwave radiometer, elastic lidar and Doppler lidar estimations in Southern Iberian Peninsula, Atmospheric Research, 213, 185–195, https://doi.org/10.1016/j.atmosres.2018.06.007, 2018.

Du, C., Liu, S., Yu, X., Li, X., Chen, C., Peng, Y., Dong, Y., Dong, Z., and Wang, F.: Urban boundary layer height characteristics and relationship with particulate matter mass concentrations in Xi'an, central China, Aerosol and Air Quality Research, 13, 1598–1607, https://doi.org/10.4209/aaqr.2012.10.0274, 2013.

Duff, P., Mariani, Z., Galarneau, E., Leroyer, S., Lauer, A., Singh, S., Gordon, M., Crawford, R., and Strong, K.: Replication Data for: Estimating planetary boundary layer height using Doppler lidar, https://doi.org/10.5683/SP4/N63T8Y, 2026.

Duncan Jr, J. B., Bianco, L., Adler, B., Bell, T., Djalalova, I. V., Riihimaki, L., Sedlar, J., Smith, E. N., Turner, D. D., Wagner, T. J., et al.: Evaluating convective planetary boundary layer height estimations resolved by both active and passive remote sensing instruments

https://doi.org/10.5194/egusphere-2026-6344
Preprint. Discussion started: 9 November 2026
© Author(s) 2026. CC BY 4.0 License.

during the CHEESEHEAD19 field campaign, Atmospheric Measurement Techniques, 15, 2479–2502, https://doi.org/10.5194/amt-15-2479-2022, 2022.

ECCC: Study of Winter Air Pollution in Toronto: Science Plan 2024 , https://www.canada.ca/en/environment-climate-change/services/air-pollution/research-science/applications/study-winter-air-pollution-toronto-science-plan/science-plan.html, 2024.

Emeis, S., Schafer, K., and Munkel, C.: Surface-based remote sensing of the mixing-layer height-a review, Meteorologische Zeitschrift, 17, 621, https://doi.org/10.1127/0941-2948/2008/0312, 2008.

Fast, J. D. and Darby, L. S.: An evaluation of mesoscale model predictions of down-valley and canyon flows and their consequences using Doppler lidar measurements during VTMX 2000, Journal of Applied Meteorology, 43, 420–436, https://doi.org/10.1175/1520-0450(2004)043<0420:AEOMMP>2.0.CO;2, 2004.

Foskinis, R., Gini, M. I., Kokkalis, P., Diapouli, E., Vratolis, S., Granakis, K., Zografou, O., Komppula, M., Vakkari, V., Nenes, A., et al.: On the relation between the planetary boundary layer height and in situ surface observations of atmospheric aerosol pollutants during spring in an urban area, Atmospheric Research, 308, 107 543, https://doi.org/10.1016/j.atmosres.2024.107543, 2024.

Frehlich, R. G. and Kavaya, M. J.: Coherent laser radar performance for general atmospheric refractive turbulence, Applied optics, 30, 5325–5352, https://doi.org/10.1364/AO.30.005325, 1991.

Heffter, J. L.: Transport Layer Depth Calculations, Second Joint Conference on Applications of Air Pollution Meteorology, AMS/APCA Second Joint Conference on Applications of Air Pollution Meteorology, 61, 65 – 98, https://doi.org/10.1175/1520-0477-61.1.65, 1980.

Hegarty, J. D., Lewis, J., McGrath-Spangler, E. L., Henderson, J., Scarino, A. J., DeCola, P., Ferrare, R., Hicks, M., Adams-Selin, R. D., and Welton, E. J.: Analysis of the planetary boundary layer height during DISCOVER-AQ Baltimore–Washington, DC, with lidar and high-resolution WRF modeling, Journal of Applied Meteorology and Climatology, 57, 2679–2696, https://doi.org/10.1175/JAMC-D-18-0014.1, 2018.

Hennemuth, B. and Lammert, A.: Determination of the atmospheric boundary layer height from radiosonde and lidar backscatter, Boundary-Layer Meteorology, 120, 181–200, https://doi.org/10.1007/s10546-005-9035-3, 2006.

Hersbach, H., Bell, B., Berrisford, P., Hirahara, S., Horányi, A., Muñoz-Sabater, J., Nicolas, J., Peubey, C., Radu, R., Schepers, D., et al.: The ERA5 global reanalysis, Quarterly Journal of the Royal Meteorological Society, 146, 1999–2049, https://doi.org/10.1002/qj.3803, 2020.

Jackson, R., O'Brien, J. R., Wang, J., Fytanidis, D. K., Kotamarthi, V. R., Muradyan, P., Grover, M., Raut, B. A., Collis, S., Tuftedal, M., Anderson, G., Wagner, T. J., Nesbitt, S. W., Tan, H., Wefer, D., and Hammond, M.: The thermodynamic and kinematic structure of the planetary boundary layer for a summer lake breeze day in Chicago, Authorea Preprints, https://doi.org/10.1029/2025JD046032, 2025.

Johansson, C., Hennemuth, B., Bösenberg, J., Linné, H., and Smedman, A.-s.: Double-layer structure in the boundary layer over the Baltic Sea, Boundary-layer meteorology, 114, 389–412, https://doi.org/10.1007/s10546-004-1671-5, 2005.

Kennedy, S.: astral, https://astral.readthedocs.io/en/latest/.

Kim, S.-W., Yoon, S.-C., Won, J.-G., and Choi, S.-C.: Ground-based remote sensing measurements of aerosol and ozone in an urban area: A case study of mixing height evolution and its effect on ground-level ozone concentrations, Atmospheric Environment, 41, 7069–7081, https://doi.org/10.1016/j.atmosenv.2007.04.063, 2007.

Krishnamurthy, R., Fernando, H., Alappattu, D., Creegan, E., and Wang, Q.: Observations of offshore internal boundary layers, Journal of Geophysical Research: Atmospheres, 128, e2022JD037 425, https://doi.org/10.1029/2022JD037425, 2023.

Lammert, A. and Bösenberg, J.: Determination of the convective boundary-layer height with laser remote sensing, Boundary-Layer Meteorology, 119, 159–170, https://doi.org/10.1007/s10546-005-9020-x, 2006.

https://doi.org/10.5194/egusphere-2026-6344
Preprint. Discussion started: 9 November 2026
© Author(s) 2026. CC BY 4.0 License.

Lenschow, D. H., Wulfmeyer, V., and Senff, C.: Measuring second-through fourth-order moments in noisy data, Journal of Atmospheric and Oceanic technology, 17, 1330–1347, https://doi.org/10.1175/1520-0426(2000)017<1330:MSTFOM>2.0.CO;2, 2000.

Leroyer, S. and Lauer, A.: Improving Subkilometer Modelling with GEM: case of Paris, in: Copernicus Meetings, https://doi.org/10.5194/icuc12-911, 2025.

Leroyer, S., Bélair, S., Husain, S. Z., and Mailhot, J.: Subkilometer numerical weather prediction in an urban coastal area: A case study over the Vancouver metropolitan area, Journal of Applied Meteorology and Climatology, 53, 1433–1453, https://doi.org/10.1175/JAMC-D-13-0202.1, 2014.

Leroyer, S., Bélair, S., Souvanlasy, V., Vallée, M., Pellerin, S., and Sills, D.: Summertime assessment of an urban-scale numerical weather prediction system for Toronto, Atmosphere, 13, 1030, https://doi.org/10.3390/atmos13071030, 2022.

Lewis, J. R., Welton, E. J., Molod, A. M., and Joseph, E.: Improved boundary layer depth retrievals from MPLNET, Journal of Geophysical Research: Atmospheres, 118, 9870–9879, https://doi.org/10.1002/jgrd.50570, 2013.

Liu, F., Yi, F., Yin, Z., Zhang, Y., He, Y., and Yi, Y.: Measurement report: characteristics of clear-day convective boundary layer and associated entrainment zone as observed by a ground-based polarization lidar over Wuhan (30.5○ N, 114.4○ E), Atmospheric Chemistry and Physics, 21, 2981–2998, https://doi.org/10.5194/acp-21-2981-2021, 2021.

Liu, S. and Liang, X.-Z.: Observed diurnal cycle climatology of planetary boundary layer height, Journal of Climate, 23, 5790–5809, https://doi.org/10.1175/2010JCLI3552.1, 2010.

Ma, W., Ma, W., Xie, Z., Wang, B., Shi, H., Woolway, R. I., and Ma, Y.: Unique atmospheric boundary layer structures driven by lake effects, Communications Earth Environment, 7, https://doi.org/10.1038/s43247-026-03234-3, 2026.

Mariani, Z., Dehghan, A., Gascon, G., Joe, P., Hudak, D., Strawbridge, K., and Corriveau, J.: Multi-instrument observations of prolonged stratified wind layers at Iqaluit, Nunavut, Geophysical Research Letters, 45, 1654–1660, https://doi.org/10.1002/2017GL076907, 2018a.

Mariani, Z., Dehghan, A., Joe, P., and Sills, D.: Observations of lake-breeze events during the Toronto 2015 Pan-American Games, Boundary-Layer Meteorology, 166, 113–135, https://doi.org/10.1007/s10546-017-0289-3, 2018b.

Mariani, Z., Crawford, R., Casati, B., and Lemay, F.: A multi-year evaluation of Doppler lidar wind-profile observations in the Arctic, Remote Sensing, 12, 323, https://doi.org/10.3390/rs12020323, 2020.

Mariani, Z., Brunet, B., Crawford, R., Reed, R., Holden, S., Sung, K., Michelson, D., Sills, D., Weaver, D., Wang, J., Shrestha, B., Su, Y., Nguyen, C., Bliankinshtein, N., and Wong, K.: The Southern Ontario Lidar (SOLID) Mesonet: Wind and Water Vapour Profiling for Aviation and Regional Nowcasting, Journal of Atmospheric and Oceanic Technology, https://doi.org/10.1175/JTECH-D-25-0102.1, 2026.

McTaggart-Cowan, R., Vaillancourt, P. A., Zadra, A., Chamberland, S., Charron, M., Corvec, S., Milbrandt, J. A., Paquin-Ricard, D., Patoine, A., Roch, M., et al.: Modernization of atmospheric physics parameterization in Canadian NWP, Journal of Advances in Modeling Earth Systems, 11, 3593–3635, https://doi.org/10.1029/2019MS001781, 2019.

Meteostat: Buffalo Airport Weather History and Climate, https://meteostat.net/en/station/72528, 2026.

NOAA: University of Wyoming Atmospheric Science Radiosonde Archive, https://weather.uwyo.edu/upperair/sounding.shtml, 2026.

Oak, Y. J., Park, R. J., Schroeder, J. R., Crawford, J. H., Blake, D. R., Weinheimer, A. J., Woo, J.-H., Kim, S.-W., Yeo, H., Fried, A., et al.: Evaluation of simulated O3 production efficiency during the KORUS-AQ campaign: Implications for anthropogenic NOx emissions in Korea, Elem Sci Anth, 7, 56, https://doi.org/10.1525/elementa.394, 2019.

Pan, K., Tangborn, A., Anderson, J. L., Santanello, J. A., Carroll, B. J., Demoz, B., and Arellano, A. F.: Assimilation of Doppler Lidar-Derived Planetary Boundary Layer Height Measurements Using an Ensemble Kalman Filter: Case Studies during the PECAN Field Campaign, Journal of Applied Meteorology and Climatology, 64, 1467–1487, https://doi.org/10.1175/JAMC-D-25-0029.1, 2025.

https://doi.org/10.5194/egusphere-2026-6344
Preprint. Discussion started: 9 November 2026
© Author(s) 2026. CC BY 4.0 License.

Park, S., Kim, M.-H., Yeo, H., Shim, K., Lee, H.-J., Kim, C.-H., Song, C.-K., Park, M.-S., Shimizu, A., Nishizawa, T., et al.: Determination of mixing layer height from co-located lidar, ceilometer and wind Doppler lidar measurements: Intercomparison and implications for PM2. 5 simulations, Atmospheric Pollution Research, 13, 101 310, https://doi.org/10.1016/j.apr.2021.101310, 2022.

Quan, J., Gao, Y., Zhang, Q., Tie, X., Cao, J., Han, S., Meng, J., Chen, P., and Zhao, D.: Evolution of planetary boundary layer under different weather conditions, and its impact on aerosol concentrations, Particuology, 11, 34–40, https://doi.org/10.1016/j.partic.2012.04.005, 2013.

Riberio, F. N., de Oliveria, A. P., Soares, J., de Miranda, R. M., Barlage, M., and Chen, F.: Effect of sea breeze propagation on the urban boundary layer of the metropolitan region of Sao Paulo, Brazil, Atmospheric Research, 214, 174–188, https://doi.org/10.1016/j.atmosres.2018.07.015, 2018.

Rye, B. J.: Refractive-turbulence contribution to incoherent backscatter heterodyne lidar returns, Journal of the Optical Society of America, 71, 687–691, https://doi.org/10.1364/JOSA.71.000687, 1981.

Scarino, A. J., Obland, M., Fast, J. D., Burton, S., Ferrare, R., Hostetler, C. A., Berg, L. K., Lefer, B., Haman, C., Hair, J., et al.: Comparison of mixed layer heights from airborne high spectral resolution lidar, ground-based measurements, and the WRF-Chem model during CalNex and CARES, Atmospheric Chemistry and Physics, 14, 5547–5560, https://doi.org/10.5194/acp-14-5547-2014, 2014.

Schween, J., Hirsikko, A., Löhnert, U., and Crewell, S.: Mixing-layer height retrieval with ceilometer and Doppler lidar: from case studies to long-term assessment, Atmospheric Measurement Techniques, 7, 3685–3704, https://doi.org/10.5194/amt-7-3685-2014, 2014.

Seibert, P., Beyrich, F., Gryning, S.-E., Joffre, S., Rasmussen, A., and Tercier, P.: Review and intercomparison of operational methods for the determination of the mixing height, Atmospheric Environment, 34, 1001–1027, https://doi.org/10.1016/S1352-2310(99)00349-0, 2000.

Seidel, D. J., Zhang, Y., Beljaars, A., Golaz, J.-C., Jacobson, A. R., and Medeiros, B.: Climatology of the planetary boundary layer over the continental United States and Europe, Journal of Geophysical Research: Atmospheres, 117, https://doi.org/10.1029/2012JD018143, 2012.

Stull, R. B.: An introduction to boundary layer meteorology, vol. 13, Springer Science & Business Media, 2012.

Su, T., Li, Z., Zheng, Y., Luan, Q., and Guo, J.: Abnormally shallow boundary layer associated with severe air pollution during the COVID-19 lockdown in China, Geophysical Research Letters, 47, e2020GL090 041, https://doi.org/10.1029/2020GL090041, 2020.

Tangborn, A., Demoz, B., Carroll, B. J., Santanello, J., and Anderson, J. L.: Assimilation of lidar planetary boundary layer height observations, Atmospheric Measurement Techniques, 14, 1099–1110, 2021.

Taylor, G. I.: Statistical theory of turbulence, Proceedings of the Royal Society of London. Series A-Mathematical and Physical Sciences, 151, 421–444, https://doi.org/10.1098/rspa.1935.0158, 1935.

Tucker, S. C., Senff, C. J., Weickmann, A. M., Brewer, W. A., Banta, R. M., Sandberg, S. P., Law, D. C., and Hardesty, R. M.: Doppler lidar estimation of mixing height using turbulence, shear, and aerosol profiles, Journal of Atmospheric and Oceanic Technology, 26, 673–688, https://doi.org/10.1175/2008JTECHA1157.1, 2009.

Vaisala: Vaisala Ceilometer CL51 User's Guide, 2010.

Vogelezang, D. and Holtslag, A.: Evaluation and model impacts of alternative boundary-layer height formulations, Boundary-Layer Meteorology, 81, 245–269, https://doi.org/https://doi.org/10.1007/BF02430331, 1996.

Wang, M., Tang, G., Liu, Y., Ma, M., Yu, M., Hu, B., Zhang, Y., Wang, Y., and Wang, Y.: The difference in the boundary layer height between urban and suburban areas in Beijing and its implications for air pollution, Atmospheric Environment, 260, 118 552, https://doi.org/10.1016/j.atmosenv.2021.118552, 2021.

Wang, X. and Wang, K.: Homogenized Variability of Radiosonde-Derived Atmospheric Boundary Layer Height over the Global Land Surface from 1973 to 2014, Journal of Climate, 29, 6893–6908, https://doi.org/10.1175/JCLI-D-15-0766.1, 2016.

Zadra, A.: Notes on the calculation of the PBL height (H), Tech. rep., Environment and Climate Change Canada, [Internal document], 2014.

https://doi.org/10.5194/egusphere-2026-6344
Preprint. Discussion started: 9 November 2026
© Author(s) 2026. CC BY 4.0 License.



Zhao, X., Griffin, D., Fioletov, V., McLinden, C., Davies, J., Ogyu, A., Lee, S. C., Lupu, A., Moran, M. D., Cede, A., et al.: Retrieval of total column and surface NO 2 from Pandora zenith-sky measurements, Atmospheric Chemistry and Physics, 19, 10 619–10 642, https://doi.org/10.5194/acp-19-10619-2019, 2019.

Zhao, X., Fioletov, V., Griffin, D., McLinden, C., Staebler, R., Mihele, C., Strawbridge, K., Davies, J., Abboud, I., Lee, S. C., et al.: The differences between remote sensing and in situ air pollutant measurements over the Canadian oil sands, Atmospheric Measurement Techniques, 17, 6889–6912, https://doi.org/10.5194/amt-17-6889-2024, 2024.

Zilitinkevich, S. and Baklanov, A.: Calculation of the height of the stable boundary layer in practical applications, Boundary-Layer Meteorology, 105, 389–409, https://doi.org/10.1023/A:1020376832738, 2002.